TOWARD CHARACTERIZATION OF THE TYPE IIP SUPERNOVA PROGENITOR POPULATION: A STATISTICAL SAMPLE OF LIGHT CURVES FROM Pan-STARRS1

N. E. Sanders[1], A. M. Soderberg[1], S. Gezari[2], M. Betancourt[3], R. Chornock[1], E. Berger[1], R. J. Foley[4,5], P. Challis[1], M. Drout[1], R. P. Kirshner[1], R. Lunnan[1], G. H. Marion[1], R. Margutti[1], R. McKinnon[1], D. Milisavljevic[1], G. Narayan[6], A. Rest[7], E. Kankare[8], S. Mattila[8], S. J. Smartt[9], M. E. Huber[10], W. S. Burgett[10], P.W. Draper[11], K. W. Hodapp[10], N. Kaiser[10], R. P. Kudritzki[10], E. A. Magnier[10], N. Metcalfe[11], J. S. Morgan[10], P. A. Price[12], J. L. Tonry[10], R. J. Wainscoat[10], AND C. Waters[10]

[1] Harvard-Smithsonian Center for Astrophysics, 60 Garden Street, Cambridge, MA 02138, USA; nsanders@cfa.harvard.edu
[2] Department of Astronomy, University of Maryland, College Park, MD 20742-2421, USA
[3] Department of Statistics, University of Warwick, Coventry, UK
[4] Astronomy Department, University of Illinois at Urbana-Champaign, 1002 West Green Street, Urbana, IL 61801, USA
[5] Department of Physics, University of Illinois Urbana-Champaign, 1110 W. Green Street, Urbana, IL 61801, USA
[6] National Optical Astronomy Observatory, 950 North Cherry Avenue, Tucson, AZ 85719, USA
[7] Department of Physics and Astronomy, Johns Hopkins University, 3400 North Charles Street, Baltimore, MD 21218, USA
[8] Finnish Centre for Astronomy with ESO (FINCA), University of Turku, Väisäläntie 20, 21500 Piikkiö, Finland
[9] Astrophysics Research Centre, School of Mathematics and Physics, Queens University, BT7 1NN, Belfast, UK
[10] Institute for Astronomy, University of Hawaii, 2680 Woodlawn Drive, Honolulu, HI 96822, USA
[11] Department of Physics, Durham University, South Road, Durham DH1 3LE, UK
[12] Department of Astrophysical Sciences, Princeton University, Princeton, NJ 08544, USA

ABSTRACT

In recent years, wide-field sky surveys providing deep multiband imaging have presented a new path for indirectly characterizing the progenitor populations of core-collapse supernovae (SNe): systematic light-curve studies. We assemble a set of 76 *grizy*-band Type IIP SN light curves from Pan-STARRS1, obtained over a constant survey program of 4 yr and classified using both spectroscopy and machine-learning-based photometric techniques. We develop and apply a new Bayesian model for the full multiband evolution of each light curve in the sample. We find no evidence of a subpopulation of fast-declining explosions (historically referred to as "Type IIL" SNe). However, we identify a highly significant relation between the plateau phase decay rate and peak luminosity among our SNe IIP. These results argue in favor of a single parameter, likely determined by initial stellar mass, predominantly controlling the explosions of red supergiants. This relation could also be applied for SN cosmology, offering a standardizable candle good to an intrinsic scatter of $\lesssim 0.2$ mag. We compare each light curve to physical models from hydrodynamic simulations to estimate progenitor initial masses and other properties of the Pan-STARRS1 Type IIP SN sample. We show that correction of systematic discrepancies between modeled and observed SN IIP light-curve properties and an expanded grid of progenitor properties are needed to enable robust progenitor inferences from multiband light-curve samples of this kind. This work will serve as a pathfinder for photometric studies of core-collapse SNe to be conducted through future wide-field transient searches.

Key words: supernovae: general – surveys

Supporting material: machine-readable tables

1. INTRODUCTION

Core-collapse supernovae (CCSNe) mark the explosive deaths of massive stars. Several independent lines of evidence, including explosion modeling (Nadyozhin 2003; Maguire et al. 2012; Jerkstrand et al. 2014; Takáts et al. 2013), progenitor star photometry (Li et al. 2007; Smartt et al. 2009; Walmswell & Eldridge 2012), rate statistics (Smith et al. 2011), and theory (Heger et al. 2003; Ekström et al. 2012), combine to suggest a lower main-sequence initial mass (M_{in}) limit for achieving core collapse of $M_{in} \gtrsim 8$–$12\,M_\odot$. Red supergiant progenitor stars in this mass range are known to produce Type IIP (hydrogen-rich) SN explosions, the most common form of CCSNe. The upper mass limit for SN IIP progenitors is more uncertain, with stars of $M_{in} \gtrsim 16$–$30\,M_\odot$ realizing significant mass loss depending on their mass, metallicity, rotation rate, binarity, and other properties, and even more massive stars ending their lives through more exotic explosion mechanisms. These mass limits for CCSN progenitor stars have profound implications throughout stellar and galactic astrophysics, including

as an input to and constraint on models of stellar evolution for massive stars (Groh et al. 2013a; Meynet et al. 2013), chemical evolution (Timmes et al. 1995; Nomoto et al. 2006, 2013), SN feedback in the interstellar medium and galaxy formation (Leitherer et al. 1992; Stilp et al. 2013), and astrobiological planetary sterilization rates (Clark et al. 1977; Lineweaver et al. 2004).

The electromagnetic signatures of these core-collapse explosions are diverse, depending sensitively on the properties of both the core and the outer envelope of the progenitor star at the time of explosion. SNe with hydrogen features detected in their optical spectra are referred to as Type II SNe, with a variety of subtypes defined by more specific spectroscopic and/or photometric criteria (see, e.g., Filippenko 1997; Li et al. 2011). Members of the most common subclass, Type IIP, are typified by broad ($\sim 10,000$ km s^{-1}) hydrogen Balmer P Cygni spectroscopic features, fast rise times of a few days, and optical light curves dominated by a long-lived, ~ 100 day "plateau" phase of roughly constant luminosity. The plateau phase is understood to arise from hydrogen recombination in the ejecta, with cooling

temperature balancing the expansion of the blast wave to essentially equilibrate the *R*-band luminosity (see, e.g., Kasen & Woosley 2009). The Type IIL subclass is historically designated based on spectroscopic properties similar to SNe IIP, but with faster, "linearly" declining optical light curves rather than a long-lived plateau. Type IIb SNe are classified spectroscopically based on the disappearance of H features and the prominence of He absorptions. Type IIb light curves feature slow rise times and rapid decline rates (in each case, a few weeks) typical of Type I (H deficient) SNe. Members of the most extreme subclass, Type IIn, are identified by intermediate-width ($\sim 10^3$ km s^{-1}) H emission features reflecting interaction of SN ejecta with circumstellar material, and contributions from this interaction can power these explosions to reach extreme luminosities at peak.

The optical evolution of Type IIP SNe has been explored in light-curve studies by a number of authors, including Patat et al. (1994), Chieffi et al. (2003), Hamuy (2003), Nadyozhin (2003), Bersten & Hamuy (2009), Li et al. (2011), Arcavi et al. (2012), Anderson et al. (2014), Faran et al. (2014). The relationship between these observables and the properties of SN progenitor stars has been explored in theoretical parameter studies by Arnett (1980), Litvinova & Nadezhin (1985), Young (2004), Kasen & Woosley (2009), Dessart et al. (2013), and others. Combining a uniform analysis of a statistical population of SN IIP light curves with consistent physical models for inferring the properties of their stellar progenitors represents a path forward for characterizing the progenitor population.

Here we describe an analysis of a statistical sample of SN IIP light-curve properties, performed using observations from the Panoramic Survey Telescope & Rapid Response System 1 survey (Pan-STARRS1, abbreviated PS1). This represents the first such population analysis of SN IIP light curves based on a homogeneously collected and multiband photometric sample from a wide-field optical survey. In Section 2 we describe the PS1 optical observations and follow-up optical spectroscopy program used to construct the light-curve sample. We have developed a novel Bayesian methodology for self-consistently modeling the full population of light curves in the sample and obtaining robust measurements of physically meaningful light-curve parameters (Section 3). We discuss the population-wide distributions of these parameters and compare them with previous observational studies (Section 4). By comparison with theoretical light-curve models, we recover estimates of the progenitor properties of the objects in our sample and discuss the limitations of the available models in Section 5. We summarize and conclude in Section 6. In a companion paper, Sanders et al. (2014), we apply the PS1 SN II data presented here as a test case for a hierarchical Bayesian light-curve fitting methodology that enables simultaneous modeling of full populations of transient light curves.

2. OBSERVATIONS

2.1. Pan-STARRS1 Imaging

We select an SN II light-curve sample from the transients discovered and monitored by PS1 since the initiation of the survey in 2010, consisting of 18,953 relevant photometric data points, 5,096 of which are robust transient detections. PS1 is a high-etendue wide-field imaging system, designed for dedicated survey observations and located on the peak of Haleakala on the island of Maui in the Hawaiian island chain. Routine observations are conducted remotely, from the University of Hawaii—Institute for Astronomy Advanced Technology Re-

search Center (ATRC) in Pukalani. A summary of details of PS1 operations relevant to SN studies is given in Rest et al. (2014), and we discuss its key features here.

A complete description of the PS1 system, both hardware and software, is provided by Kaiser et al. (2002). The 1.8 m diameter primary mirror, 3°.3 field of view, and other PS1 optical design elements are described in Hodapp et al. (2004); the array of 60 4800 × 4800, 0″.258 pixel detectors, and other attributes of the PS1 imager is described in Tonry & Onaka (2009); and the survey design and execution strategy are described in K. C. Chambers (in preparation). The PS1 Medium Deep Survey (MDS) consists of 10 pencil-beam fields observed with a typical cadence of 3 days in each filter, to a 5σ depth of $\sim$23.3 mag in *griz* filters and $\sim$21.7 mag in the *y*-filter (with observations taken near full Moon).

The PS1 observations are obtained through a set of five broadband filters, which we refer to interchangeably as g_{P1}, r_{P1}, i_{P1}, z_{P1}, and y_{P1} or simply *grizy* (Stubbs et al. 2010). Although the filter system for PS1 has much in common with that used in previous surveys, such as the Sloan Digital Sky Survey (SDSS; York et al. 2000; Aihara et al. 2011), there are important differences. The g_{P1} filter extends 200 Å redward of g_{SDSS}, and the z_{P1} filter is cut off at 9200 Å. SDSS has no corresponding y_{P1} filter. Further information on the passband shapes is described in Stubbs et al. (2010). Photometry is in the "natural" PS1 system, $m = 2.5 \log(\text{flux}) + \text{m}'$, with a single zero-point adjustment m' made in each band to conform to the AB magnitude scale (Tonry et al. 2012).[13] We assume a systematic uncertainty of 1% for our PS1 observations owing to the asymmetric PS1 point-spread function and uncertainty in the photometric zero-point calibration (Tonry et al. 2012). See Figure 1 for an illustration of the PS1 photometric sampling and the range in data quality.

The standard reduction, astrometric solution, and stacking of the nightly images are done by the Pan-STARRS1 IPP system (Magnier 2006; Magnier et al. 2008). The nightly MDS stacks are transferred to the Harvard Faculty of Arts and Sciences "Odyssey" Research Computing cluster, where they are processed through a frame subtraction analysis using the *photpipe* image differencing pipeline developed for the SuperMACHO and ESSENCE surveys (Rest et al. 2005; Miknaitis et al. 2007; Rest et al. 2014).

2.2. Optical Spectroscopy

We begin with a selection of PS1-discovered SNe that were classified as Type II through our spectroscopic follow-up campaign: 112 objects in total. One object in our sample, PS1-10ae (SN 2010aq), has previously been reported on in Gezari et al. (2010). We note that the PS1 spectroscopic follow-up is not complete; brighter objects, those with longer plateau durations, and those with the highest ratio of SN to underlying galaxy light are most likely to be overrepresented in our sample, owing to their availability for spectroscopy.

Spectra were obtained using the Blue Channel and Hectospec spectrographs of the 6.5 m MMT telescope (Schmidt et al. 1989; Fabricant et al. 2005), the Low Dispersion Survey Spectrograph (LDSS3) and Inamori-Magellan Areal Camera and Spectrograph (IMACS; Dressler et al. 2006) of the 6.5 m Magellan telescopes, the Gemini Multi-Object Spectrograph of the 8 m Gemini telescopes (GMOS; Hook et al. 2004), and the

---

[13] The magnitudes quoted throughout this paper are in the AB system, except where explicitly noted.
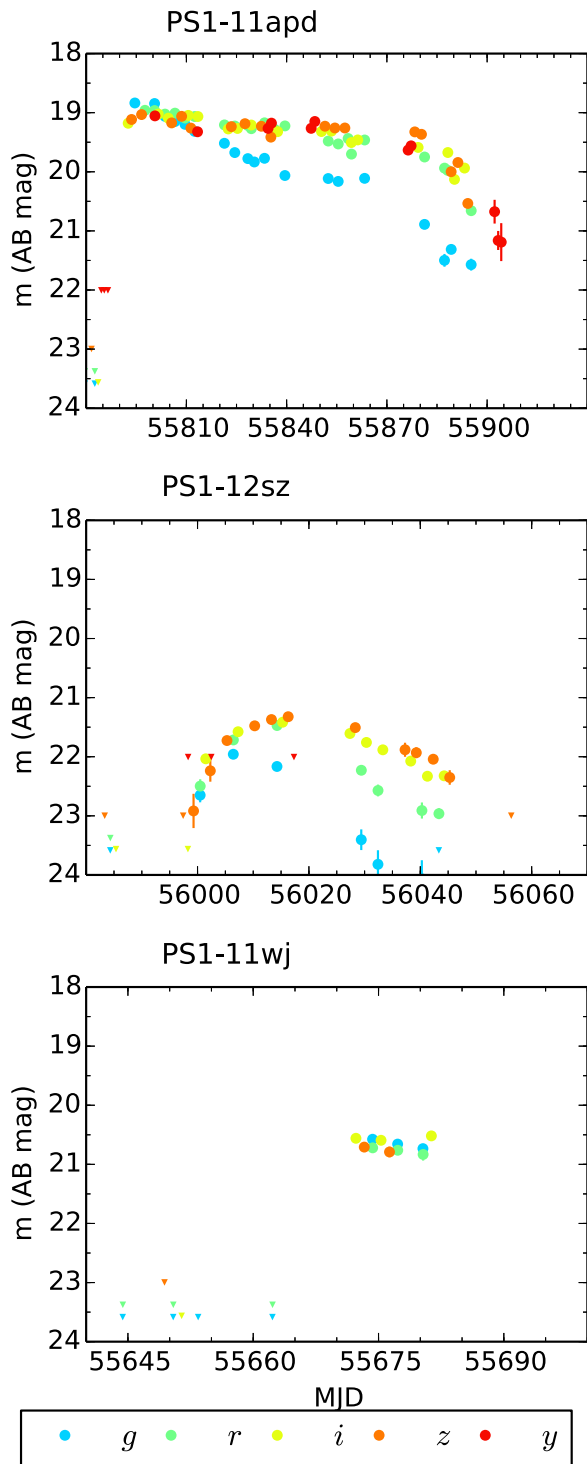
Figure 1. Sample PS1 multiband light curves from the SN II data set. Top: PS1-11apd, a bright SN IIP with a light curve sampled from peak through the plateau and the transition to the radioactive decay phase, covering ∼100 days. Middle: PS1-12sz, an SN IIb that peaked at ∼21st magnitude with a well-sampled light curve. Bottom: PS1-11wj, an SN IIP with photometry sampled only during the plateau phase. In each plot, the filters are specified by the colors shown in the legend, and the triangles represent nondetection upper limits (with values set from the 2σ level of the distribution of detected magnitudes from the full photometric data set in each filter).
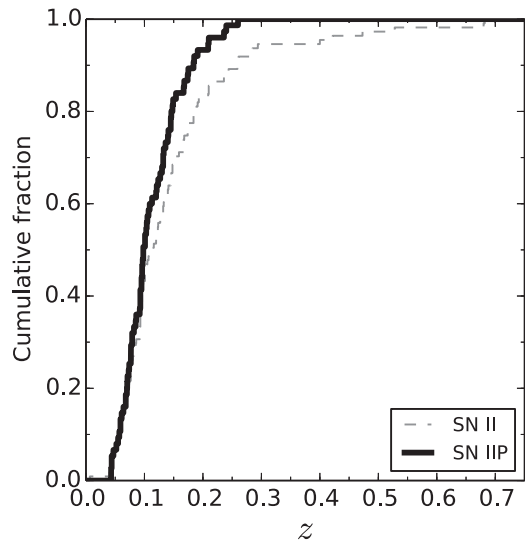
Figure 2. Cumulative redshift distribution for PS1 SNe II. The subsample classified as SNe IIP (see Section 3.4) is shown with the thick line.

IIL, IIb, and Type IIn subclasses of the SNe II; we discuss subclassification in Section 3.4.

Additionally, we obtain host galaxy redshift measurements for each object from these spectra, which we use for K-correction (see Section 2.3) and to estimate distance.[14] Figure 2 shows the host galaxy redshift distribution of the PS1 SN II sample, which has [16,50,84]th percentile values of [0.07, 0.11, 0.21]. The subsample classified as SNe IIP (see Section 3.4) has distribution percentile values of [0.07,0.10,0.16]. This difference reflects a population of luminous, distant SNe IIn excluded from the subsample.

Details of our final SN IIP sample, as described in Section 3.4, are listed in Table 1.

2.3. K-corrections

We use K-corrections to account for the difference between the observed and rest-frame wavelengths of the light collected through the PS1 filters, as a function of the redshift of each object in our sample. We define this correction as $K = m_R - M_Q - DM$, where m_R is the observed-frame magnitude, M_Q is the emitted-frame absolute magnitude, and DM is the distance modulus (Hogg et al. 2002). We estimate K-corrections using the SN IIP spectral templates provided by P. Nugent (based on observations of SN 1999em; Gilliland et al. 1999; Baron et al. 2004).[15] We interpolate linearly between the spectral templates to obtain K-corrections for arbitrary epochs. We note that we do not warp the spectral templates to match the observed color of the SN, owing to the computational cost involved in doing so dynamically within our probabilistic light-curve fitting methodology (see Appendix A). By testing the effects of warping the spectral templates on the K-correction calculation, we estimate that neglecting this effect will introduce an uncertainty of ∼0.02 mag in the K-correction per 0.1 mag of $(V - I)$ color offset, which is much smaller than typical uncertainties in our color estimates.

Figure 3 illustrates the resulting K-corrections for an illustrative set of epochs. The $t = 0$ K-correction is linear with z

Andalucia Faint Object Spectrograph and Camera (ALFOSC) at the 2.6 m Nordic Optical Telescope. Objects were classified as Type II by identification of Hα emission not associated with the host galaxy. This selection could possibly include the Type IIP,

Table 1
Pan-STARRS1 Type IIP SN Sample

PS1 SN	Field	R.A.	Decl.	Disc. MJD	z	N_g	N_r	N_i	N_z	N_y
PS1–10a	02	03:29:48.735	−29:04:29.91	55207	0.071	2	2	5	4	0
PS1–10b	03	08:37:02.587	+43:44:16.85	55207	0.260	4	4	5	0	0
PS1–10q	06	12:19:37.533	+46:01:56.03	55212	0.057	15	17	16	13	0
PS1–10t	04	09:55:30.959	+01:29:01.18	55214	0.093	11	11	11	11	0
PS1–10ae	04	10:02:09.742	+01:14:00.93	55242	0.086	4	5	8	6	0

Notes. This table includes only SNe classified as SNe IIP by the criteria of Section 3.4. PS1 SN is the PS1 designation of the transient, field is the PS1 Medium Deep Field where the transient was discovered, R.A. and decl. are in J2000 coordinates, Disc. MJD is the date of discovery, z is the redshift obtained from our follow-up spectroscopy (Section 2.2), and N_x is the number of detections of the object included in our data set in each PS1 filter (additional photometric nondetections are also used to constrain the explosion date and decay behavior).

(This table is available in its entirety in machine-readable form.)

Figure 3. Estimated SN IIP K-corrections in PS1 filters (different panels), derived as described in the text. The line colors correspond to different epochs (rest-frame days since explosion; key at top).

highly dependent on time, as the onset of line blanketing in the spectral model depresses the flux blueward of ∼5000 Å.

Deviation of the SN spectral energy distribution from the template spectra will introduce error into our derived K-correction. In particular, we consider here the effect of differences in the SN IIP continuum shape and line-of-sight extinction and estimate the magnitude of these effects by simulation on the template spectra. First, we consider the effect of variation in continuum shape, to first order. We vary the intrinsic $(V − I)$ color of the SN spectrum by ±0.5 mag from the stock template, at fixed redshift ($z = 0.1$), at fixed epoch ($t = 50$ days), and with no extinction. The effect of this variance in spectral shape on the K-correction over the full 1 mag color range induces a variation in the K-correction ranging from 0.1 mag in g band to 0.3 mag in y band. Second, we consider the effect of variation in extinction. We vary the extinction from $A_V = 0$ to 2 mag, at fixed redshift ($z = 0.1$), at fixed epoch ($t = 50$ days), and with the color of the stock template. The effect of this variance in spectral shape on the K-correction over the full 2 mag extinction range induces a variation in the K-correction ranging from 0.1 mag in y band to 0.2 mag in i band. These effects are therefore modest and similar in size, depending on the exact parameters of the photometric observation.

We estimate the typical effect of the joint variation in both continuum shape and extinction by means of Monte Carlo simulation. We generate 10,000 random SN observations with the following conditionally independent distributions of properties meant to approximately mimic the PS1 data set: redshift drawn from $z \sim \mathrm{logN}(-2, 0.4)$, color deviation drawn from $\Delta(V − I) \sim N(0, 0.5)$ mag,[16] extinction drawn from $A_V \sim \mathrm{logN}(0, 1)$ mag, and epoch drawn from $t \sim \mathrm{logN}(4, 0.8)$ days, where N is the normal and logN is the lognormal distribution. We then consider the distribution of residuals of the derived K-corrections from the K-correction expected for a zero-extinction and template-standard color object. In the r band, this distribution has [5, 16, 50, 84, 95] percentile values of [−0.10, −0.01, 0.13, 0.40, 0.75] mag. The distribution is similar in other filters. This suggests that these effects exert a small (∼0.1 mag) typical bias and introduces a modest additional uncertainty (∼0.2 mag) in the measured SN photometry. We therefore neglect these effects in the following work but note their importance for studies requiring precision photometry. In the most extreme cases, particularly for the most highly

because the postshock breakout cooling phase spectral model is a blackbody; thereafter the K-correction evolution becomes more complex, with spectral features evolving and shifting between bandpasses. The bluer bands have K-corrections more

---

[16] Our simulated $(V − I)$ color distribution is meant to provide a conservative accounting of intrinsic spectral deviance between SNe IIP. For comparison, Olivares (2008) identify an intrinsic $(V − I)$ color dispersion of <0.1 mag.
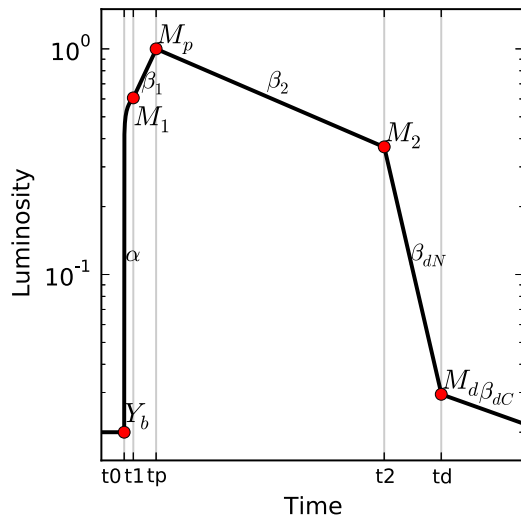
Figure 4. Schematic illustration of the five-component SN II light-curve model defined in Equation (1). The gray vertical lines denote the duration (t_x) between epochs of transition between the piecewise components of the model. The background level (Y_b) and turnover fluxes (M_x) are marked and labeled (red points). The power law (α) and exponential (β_x) rate constant for each phase are labeled adjacent to each light-curve segment.

reddened SNe, the simulations suggest that these effects will cause the brightness to be significantly underestimated (by $\gtrsim 0.7$ mag). Moreover, the simulated K-correction residuals seem to have little correlation between filters, suggesting that the effects do not significantly bias color inference.

3. LIGHT-CURVE MODELING

In order to consistently compare the photometric properties of the SN IIPs in our sample, we have produced models of the full, multiband light-curve evolution of each SN using a Bayesian methodology. We apply weakly informative priors to regularize the shape of the light-curve fits to conform to SN IIP phenomenology. The product of the modeling is a posterior predictive probability distribution for the luminosity of the SN at every phase and joint posterior probability distributions for associated light-curve parameters. This methodology enables us to model the full pseudobolometric light-curve evolution of all objects in our sample from explosion through the radioactive decay phase, regardless of variation in photometric coverage and data quality, while fully accounting for statistical uncertainty. Throughout, we interpret these marginal parameter probability distributions in the context of the influence of the weakly informative priors to avoid introducing bias on our inference.

3.1. Parameterized Light-curve Model

To model the light curve, we use a simple, physically motivated parameterization that captures the essential components of the rise, plateau, and decline phases of the Type IIP light curve. Our model is constructed so that the most salient features of the SN IIP light curve (the plateau duration, peak magnitude, and luminosity evolution of the radioactive decay phase) are represented by directly interpretable parameters.

The light-curve model for the luminosity measured from our PS1 forced photometry, l, in a given optical filter, F, consists of five piecewise components (see Figure 4): a power-law fast-rise phase, a plateau phase divided into exponential rising and declining components, a transitional phase representing the end

of the plateau, and a postplateau exponential decay phase:

$$
l[t, \ldots] = \begin{cases}
0, \\
\quad \text{if } t < t_0 \\
M_1(t/t_1)^\alpha, \\
\quad \text{if } t_0 < t < t_0 + t_1 \\
M_1 \exp(\beta_1(t - t_1)), \\
\quad \text{if } t_0 + t_1 < t < t_0 + t_1 + t_p \\
M_p \exp(-\beta_2(t - (t_p + t_1))), \\
\quad \text{if } t_0 + t_1 + t_p < t < t_0 + t_1 + t_p + t_2 \\
M_2 \exp(-\beta_{dN}(t - (t_2 + t_p + t_1))), \\
\quad \text{if } t_0 + t_1 + t_p + t_2 < t \\
\quad\quad < t_0 + t_1 + t_p + t_2 + t_d \\
M_d \exp(-\beta_{dC}(t - (t_d + t_2 + t_p + t_1))), \\
\quad \text{if } t_0 + t_1 + t_p + t_2 + t_d < t.
\end{cases} \tag{1}
$$

These parameters have the following definitions and interpretations. The time parameters are defined where t is the Modified Julian Date (MJD) epoch of an observation, t_0 is the epoch of explosion, t_1 is the rest-frame duration of the power-law rise phase, t_p is the duration of the exponential rise phase (ending at peak flux), t_2 is the duration of the falling component of the plateau phase, and t_d is the duration of the transitional phase. The flux parameters are defined such that M_1 is the flux at the transition from the power law to the exponential rise phases, M_p is the peak flux, M_2 is the flux at the end of the plateau phase, and M_d is the flux at the transition to the Co decay-dominated phase. The rate parameters are defined such that α is the power-law rise slope, β_1 is the exponential rate constant during the rising phase of the plateau, β_2 is the rate constant during the declining phase of the plateau, β_{dN} is the exponential decline rate of the transition phase following the plateau, and β_{dC} is the exponential decay constant corresponding to ^{56}Co to ^{56}Fe decay. Each parameter is defined independently for each photometric filter, with the exception of t_0. For numerical convenience, we define l in arbitrary scaled units relative to the absolute magnitude M, such that $M = -2.5 \log_{10}(10^7 \times l)$.

Note that, in order for the light-curve model to be continuous, not all of the parameters may be independent. In particular, for each filter,

$$M_1 = M_p / \exp(\beta_1 t_p) \tag{2}$$

$$M_2 = M_p / \exp(-\beta_2 t_2) \tag{3}$$

$$M_d = M_2 / \exp(-\beta_{dN} t_d). \tag{4}$$

Furthermore, we note that the postpeak decay rate β_2 is directly related to the quantity Δm_{15}, the decline in magnitudes of the light curve in the 15 days following peak:

$$\Delta m_{15} = \frac{15 \times 2.5}{\log_e 10} \beta_2 \sim 16.3 \beta_2. \tag{5}$$

Our model is similar to the linear segmented light-curve fitting approach of, e.g., Patat et al. (1993), but (as we discuss in Section 3.2) our fitting methodology for the knot properties is fully probabilistic rather than manual. We prefer this piecewise analytic formulation to the additive component model used by, e.g., Olivares (2008). The piecewise parameters will in principal have weaker covariance, therefore reducing the posterior curvature and increasing the efficiency of Markov Chain Monte Carlo (MCMC) methods for sampling from the posterior. While this parameterization is designed to capture the phenomenology of SNe IIP, it is in practice quite flexible, as we obtain reasonably descriptive fits to the light curves of other SNe II (e.g., SNe IIn and IIb).
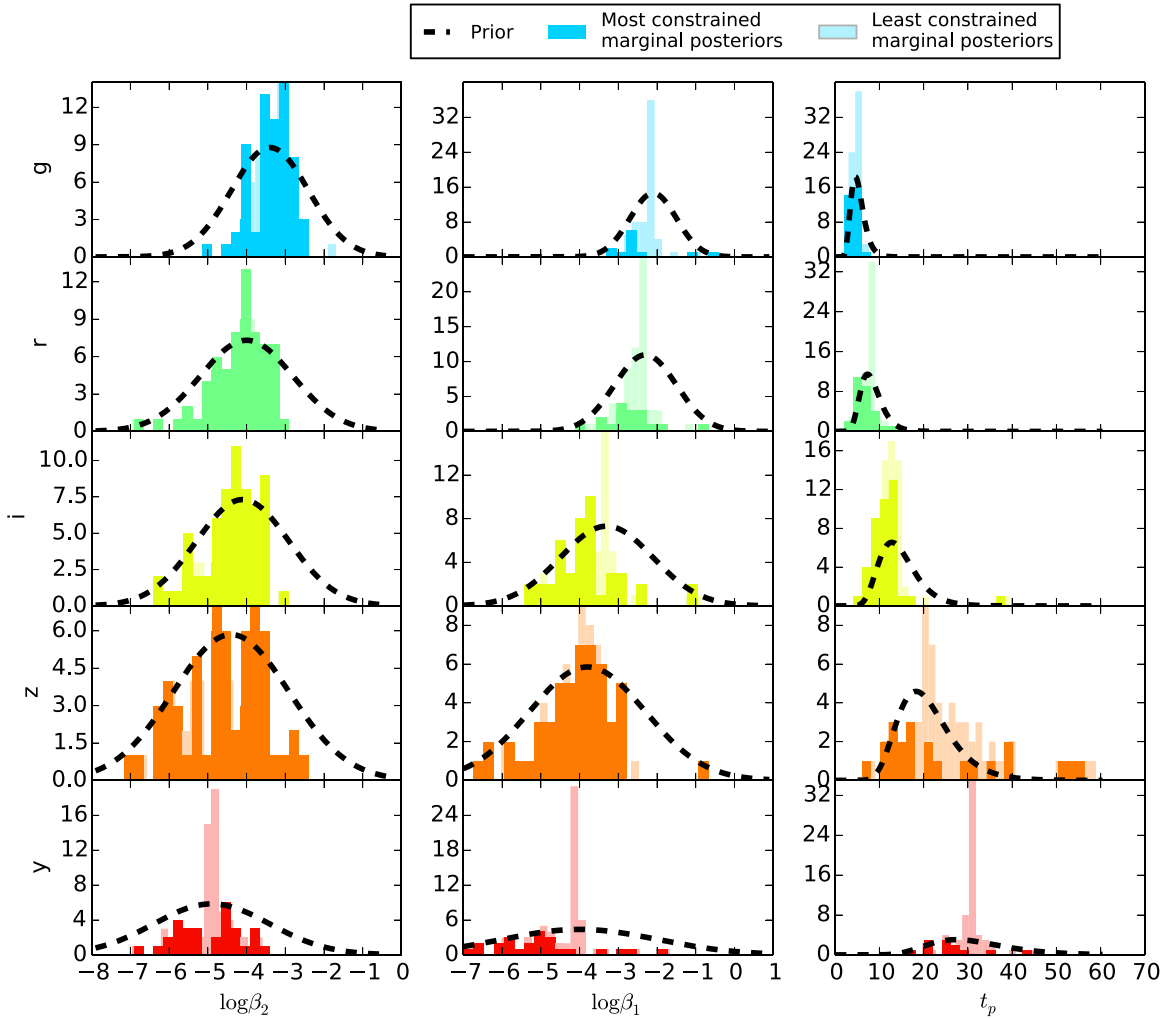
Figure 5. Illustration of prior distribution construction for parameters of the Bayesian SN IIP light-curve model. Filters are displayed by row; parameters, by column. Only parameters with priors defined per filter are shown. The bars show the distribution of the marginalized posterior medians for the fitted light-curve model parameters. The least constrained posterior medians (with variance 80% or more of the variance in the prior) are shown with the faded bars, and more constrained posterior medians are shown with darker bars. The chosen prior distribution is shown with the dashed lines. Posteriors fitted exclusively with information from the prior (no constraint provided by the data, e.g., the least constrained marginal posteriors) would appear exactly at the position of the prior mean.

Table 2
Pan-STARRS1 Type IIP SN Light-curve Parameters

SN	t_0	$\log \alpha$	$\log \beta_1$	$\log \beta_2$	$\log \beta_{dN}$	$\log \beta_{dC}$	t_1	t_p	t_2	t_d	M_p	V
						g-band						
PS1–10a	$55200.9^{+0.8}_{-0.8}$	$-1.0^{+0.3}_{-0.3}$	$-2.4^{+0.5}_{-0.5}$	$-3.1^{+0.3}_{-0.4}$	$-2.9^{+0.5}_{-0.5}$	$-5.0^{+1.2}_{-1.1}$	$1.0^{+0.3}_{-0.2}$	5^{+1}_{-1}	106^{+33}_{-25}	10^{+7}_{-4}	$2.10^{+0.45}_{-0.25}$	$0.005^{+0.006}_{-0.003}$
PS1–10b	$55204.0^{+0.4}_{-0.5}$	$-1.0^{+0.3}_{-0.3}$	$-2.8^{+0.3}_{-0.3}$	$-2.7^{+0.2}_{-0.2}$	$-3.0^{+0.5}_{-0.5}$	$-4.9^{+1.0}_{-1.1}$	$1.0^{+0.3}_{-0.3}$	7^{+1}_{-1}	102^{+38}_{-28}	10^{+6}_{-4}	$1.93^{+0.11}_{-0.10}$	$0.008^{+0.017}_{-0.006}$
PS1–10q	$55200.4^{+0.7}_{-0.7}$	$-1.0^{+0.3}_{-0.3}$	$-2.4^{+0.5}_{-0.5}$	$-3.1^{+0.0}_{-0.0}$	$-2.9^{+0.5}_{-0.6}$	$-4.9^{+1.0}_{-1.0}$	$1.0^{+0.4}_{-0.3}$	4^{+1}_{-1}	109^{+31}_{-24}	10^{+8}_{-4}	$0.77^{+0.03}_{-0.03}$	$0.016^{+0.004}_{-0.003}$
PS1–10t	$55205.2^{+0.9}_{-0.8}$	$-1.0^{+0.3}_{-0.3}$	$-2.2^{+0.6}_{-0.5}$	$-3.5^{+0.1}_{-0.1}$	$-3.1^{+0.5}_{-0.4}$	$-5.1^{+1.1}_{-0.9}$	$1.0^{+0.3}_{-0.3}$	5^{+1}_{-1}	97^{+32}_{-24}	10^{+7}_{-4}	$0.37^{+0.02}_{-0.02}$	$0.011^{+0.007}_{-0.007}$
PS1–10ae	$55239.3^{+0.1}_{-0.1}$	$-1.1^{+0.3}_{-0.3}$	$-2.7^{+0.5}_{-0.5}$	$-3.3^{+0.1}_{-0.1}$	$-3.0^{+0.5}_{-0.5}$	$-5.6^{+0.7}_{-0.7}$	$0.9^{+0.2}_{-0.2}$	3^{+1}_{-0}	76^{+24}_{-22}	10^{+5}_{-4}	$0.84^{+0.02}_{-0.02}$	$0.005^{+0.006}_{-0.003}$

Notes. Light-curve parameters are listed separately for each photometric band, in sequence. The parameters are defined in Section 3.1. This table includes only SNe classified as SNe IIP by the criteria of Section 3.4.

(This table is available in its entirety in machine-readable form.)

3.2. Fitting Methodology

We estimate the posterior distributions of these model parameters using an MCMC method. We employ the C++ library *Stan* (Stan Development Team 2014a), which implements the adaptive Hamiltonian Monte Carlo (HMC) *No-U-Turn Sampler* of

Hoffman & Gelman (2014). For each multiband SN light curve, we use *Stan* to return 1000 samples (250 samples each from four independent MCMC chains) from the posterior distribution of the model.[17]

---

[17] The full *Stan* code for our statistical model is discussed in Appendix A.

In addition to the light-curve parameterization outlined in Section 3, our *Stan* model includes certain features representing the data acquisition process. To account for uncertainty in the PS1 background template subtractions, we fit for the background level in each filter using an independent set of luminosity parameters, $Y_b[F]$, and an intrinsic model variance, $V[F]$. We precompute K-correction curves for the redshift of each object in our sample (see Section 2.3) and apply them to the model during the likelihood calculation using the phases corresponding to the sampled explosion date at each step in the MCMC chain.

We employ weakly informative priors (see, e.g., Gelman et al. 2008) to regularize the fitted models to the characteristic SN IIP light-curve shape. These prior distributions are constructed to more than encompass the observed variance in parameter values from well-identified light curves in the data set. The *Stan* model in Appendix A fully defines the fixed prior distributions we employ, and we discuss their most salient properties here. Figure 5 illustrates the procedure for constructing the prior distributions that we have defined individually per filter in the model. For t_2, we apply a (lognormal) $\log N(\log(100), 0.3)$ day prior. Together with our prior on t_p (Figure 5), this effectively provides a prior on the plateau duration that has [5, 50, 95]th percentile values of [70, 110, 180] days in i band (and similar values in other bands). This prior is constructed to be weakly informative, having significantly more variance than previously reported SN IIP plateau duration distributions (Arcavi et al. 2012) and covering a range of values similar to that predicted from theoretical modeling (Kasen & Woosley 2009). Perhaps the most informative prior we apply is that on the peak-magnitude distribution, which is observationally motivated. A strong prior is desirable for this parameter because it has the effect of regularizing the light-curve shape in cases where photometric observations before peak are not available. We set this prior to $N(-17.5 \text{ mag}, 0.8 \text{ mag})$ to approximately match the SN II luminosity function predicted for an R-band magnitude-limited survey by Li et al. (2011) based on observations from the Lick Observatory Supernova Search (LOSS; Figure 6).[18]

In total, including the independent parameters for each light-curve segment and filter, the fitted model for each SN has 61 independent parameters (12 per filter and t_0). We reproduce the fitted light-curve parameters for each object in our sample in Table 2.

3.3. Fitting Validation

Following execution of *Stan* and posterior sampling, we reconstruct a posterior predictive distribution for each light curve from the model parameter samples (Gelman et al. 2013). This distribution represents the probability for the physical SN light curve to have the luminosity l_m on a grid of times t_m.

Figure 7 illustrates a posterior predictive check for the model fit to the object PS1-11apd, whose well-sampled observations illustrate both the strengths and weaknesses of the five-component model. The rising phase in each band is wellconstrained by the tightest pre-explosion limit, in the y band. The two-component (rising then falling) plateau phase provides an accurate description of the data in the i band, but not in the g band, where the evolution of iron line blanketing (see, e.g., Kasen & Woosley
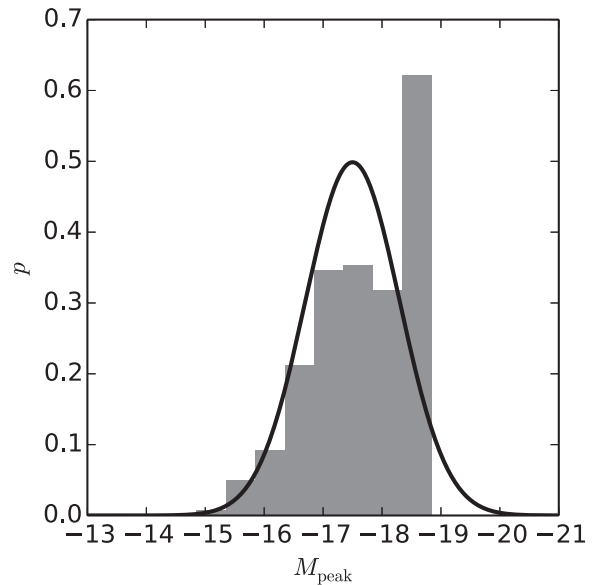
Figure 6. Prior adopted for the SN II peak magnitude distribution (solid line) compared with the observed SN II luminosity function determined by Li et al. (2011) for an ideal, magnitude-limited survey with a 1 day cadence (their Figure 10), shown with gray bars.

2009) causes a behavior not captured by the model (falling then rising/plateauing). As is characteristic of the PS1 data, the y-band light curve is more poorly sampled and higher in variance than the other bands. In general, the model parameter inferences are therefore more reliable and directly interpretable in the r, i, and z bands.

Figure 8 illustrates fitting behavior for a well-sampled and a poorly sampled PS1 light curve. The top panel shows PS1-12bku, an SN with observations from the rise phase through the end of the plateau. Note that the nonlinear behavior of the light curve during the rise, due to shock breakout and postshock breakout cooling envelope effects (see, e.g., Nakar & Sari 2010; Rabinak & Waxman 2011), is not captured by the power-law rise model, but the explosion epoch itself is fit accurately in the fitted model. PS1-10zu is shown in the bottom panel, an object that apparently exploded during the gap between observing seasons. With observations only available starting a few weeks before the end of the plateau phase and no direct constraints on the explosion epoch, the model fit includes a range of possible explosion dates reflecting the prior distributions for the plateau duration and peak magnitude.

3.4. Type II SN Subclassification

We apply a supervised machine learning methodology (see, e.g., Faraway et al. 2014) to classify the SNe II in this sample into their appropriate subclasses and, in particular, to identify SNe IIP for further analysis. Our approach is to first apply "expert knowledge" to manually label a subset of clearly classifiable objects from our sample of 112 SNe II, then uniformly measure light-curve features using the methodology described in Section 3.1, then train a Support Vector Machine (SVM) classifier to a deliberately selected subset of these features, and finally apply that classifier to assign labels to the remaining objects in the sample. In general, spectral classification of distant ($z \gtrsim 0.1$) transients is complicated by spectral evolution (see, e.g., Milisavljevic et al. 2013 for a discussion of SNe IIb), exacerbated by the observational cost of obtaining a well-sampled

---

[18] Note that Li et al. (2011) treat the SN II population as a mixture of relatively low luminosity and relatively luminous SNe (referred to as Type IIP and IIL, respectively), leading to a bimodal luminosity function as in Figure 6. Here we assume a unimodal Gaussian prior wide enough to encompass both modes of the Li et al. (2011) luminosity function, and we investigate the possibility of multimodality in the observed properties of the SNe II in Section 4.2.
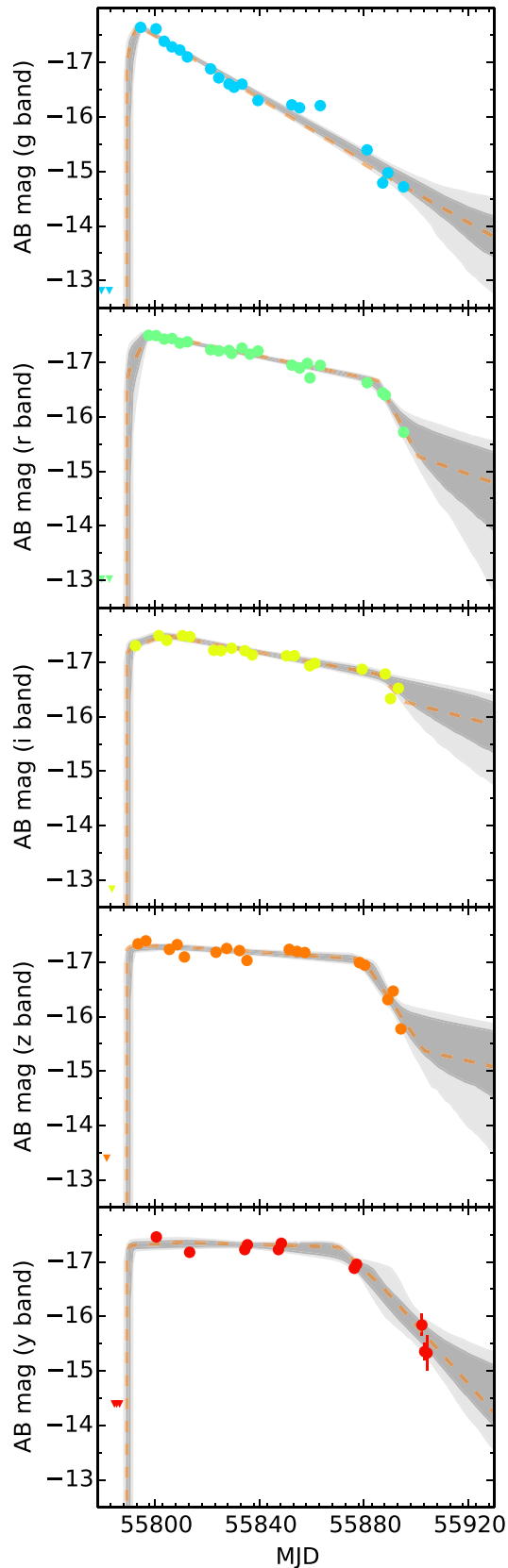
Figure 7. Example of the five-component SN II light-curve model fit to the SN PS1-11apd in each of the *grizy* bands (top to bottom). The PS1 photometry and uncertainties in each of five optical bands are displayed by the circles and error bars. The model posterior distribution is displayed by the shaded intervals; the shading boundaries correspond to the [5, 16, 84, 95]th percentile values of the posterior. The maximum likelihood model in each band is displayed by the dashed line. *K*-corrections have been applied to both the data and model, but not reddening correction. The triangles denote photometric upper limits.
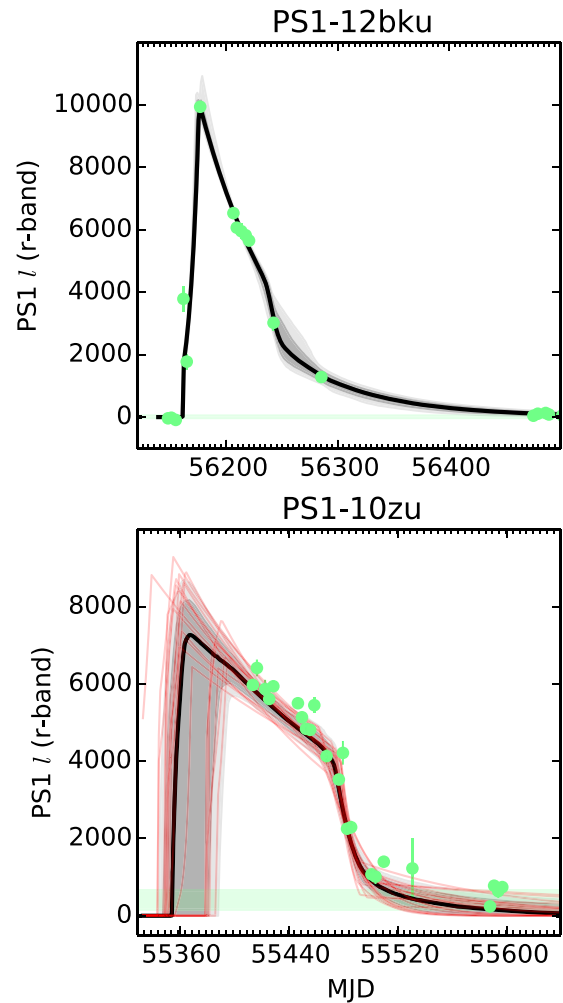
Figure 8. Examples of fitting the five-component SN II light-curve model defined in Equation (1) over a range in light-curve quality. Top: *r*-band photometry for the SN IIP PS1-12bku (green points and error bars), showing clear detections during each of the five phases on the light-curve model. The shaded areas show the 1σ and 2σ confidence intervals for the posterior distribution of the model (see Section 3.2), and the solid black line shows the median of that confidence interval. The horizontal green bar shows the range fitted for the zero-point flux offset. Bottom: same as the top panel, but for PS1-10zu. In this case, no observations constrain the rise phase, and models with a diversity of plateau durations and rise behaviors are explored by the MCMC chain (a sampling of these models is shown in red).

spectral series, and the difficulty in robustly identifying spectral features, exacerbated by the low signal-to-noise ratio of the spectroscopy relative to nearby objects. The methodology discussed below is intended to capitalize on photometric information to help overcome these limitations.

Our procedure is as follows. We begin by manually assigning SN IIP, IIb, IIn, and "II?" (undetermined) classifications to each object in the sample by inspection of their light curves and optical spectra. See, e.g., Li et al. (2011) for a discussion of the photometric and spectroscopic properties of SN II subclasses. We do not establish a label for SNe IIL separate from SNe IIP, but we discuss that subclass later in Section 4.2. We assign SN IIn classifications to 23 objects based on the detection of intermediate-width H emission features and/or exceptional luminosity ($\lesssim -20$ mag); SN IIb classifications to 5 objects based on the detection of He features (in addition to broad H features) in the optical spectrum and/or an SN I-like light curve, with slow rise and fast decline rate; and SN IIP to 67 objects based on

on the presence of a broad $H\alpha$ spectral feature and/or a clearly exhibited plateau-like light curve. Finally, we liberally apply the SN II? classification to 17 objects for which we do not have sufficient data to assign a classification and/or that do not neatly fit the preceding criteria.

We apply our Bayesian light-curve model (Section 3.1) to uniformly measure features of the light curves of every SN II in our PS1 sample. To mirror our expert knowledge, we focus on the peak absolute magnitude (M), the rise time to peak magnitude (t_p), and the postpeak decay rate (β_2) as features capable of distinguishing objects in these subclasses. We identify the i band as the filter in which these features are most discriminating. For self-consistency, we apply the SN IIP theoretical K-corrections (Section 2.3) to every object in the sample.

We then fit a linear SVM classifier (Pedregosa et al. 2011) to the features of the training set. The SVM consists of a series of hyperplanes that optimally divide the feature space to discriminate the training set based on their class labels. The results of this fit are displayed in Figure 9. In summary, the classifier identifies SNe IIn as luminous (primarily $M_i < -18$ mag) and slowly evolving ($\log \beta_2 \lesssim -3$), SNe IIb as intermediate-luminosity and quickly evolving, and SNe IIP as slowly evolving and spanning a range from subluminous ($M_i > -17$ mag) to luminous ($M_i \sim -20$ mag), accurately reflecting our expert knowledge applied in construction of the training set. Disagreement between object location and shaded labeling in Figure 9 is partially due to variance in the observational data, which limits the efficiency of the classifier, and partially due to the coarse binning of the display slices. We have configured the classifier with the penalty parameter $C = 1$ and class weights calculated from their representation in the training set.

Finally, we apply the classifier to the unclassified (SNII?) objects to infer their subclasses. While "SN IIb" and "IIn" classifications can only be assigned by spectroscopy, by definition, here we are using photometric information to supplement available spectroscopy for the purpose of predicting the most likely spectroscopic subclassification. The classifier identifies 9 of these objects as SNe IIP, which we hereafter incorporate in our SN IIP sample; 6 as SNe IIb; and 3 as SNe IIn.

When applied to the training set, the classifier achieves 83% accuracy across all subtypes, and 89% accuracy for SNe IIP. It mistakenly classifies SNe IIb and IIn as SNe IIP only 22% of the time (the false identification rate) and mistakenly classifies SNe IIP as other classes only 11% of the time (the false negative rate). These statistics imply that, of our sample of 17 SNe II?, $\sim$3 may be incorrectly classified as SNe IIP and $\sim$3 legitimate SNe IIP may be inadvertently excluded. In combination with our sample of 67 securely identified SNe IIP, this level of false identification would imply a $\sim$4% contamination rate within the sample. Given the relatively low signal-to-noise ratio of the SN II? objects, the classifier may perform more poorly than on the training data set, but for the same reason, the influence of these objects on our light-curve parameter inferences will be correspondingly suppressed.

4. RESULTS

In this section we present the results of our analysis of the observational properties of the PS1 SN IIP light curves. The parameters calculated for individual objects are summarized in Table 5.
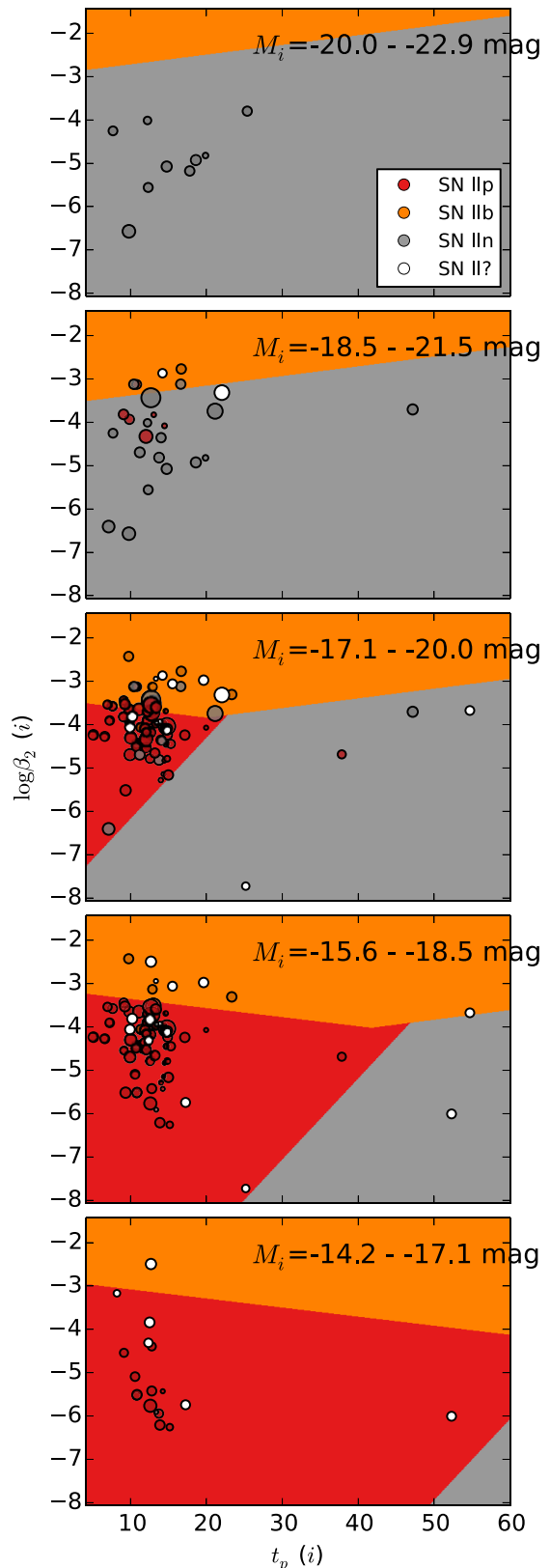
Figure 9. SVM classifier trained to the SN II light-curve feature data. The subplots display five slices of the three-dimensional feature space (β_2, t_p, M_i), representing different bins of absolute i-band magnitude. The shaded regions indicate the labeling regimes identified by the classifier, and the points represent observed objects from the sample of different manually assigned subclasses. The colored points represent the training set, and the white ("SNII?") points represent the objects to be classified. The point size reflects the uncertainty in the feature posterior distribution for each object, with larger points indicating smaller uncertainty.
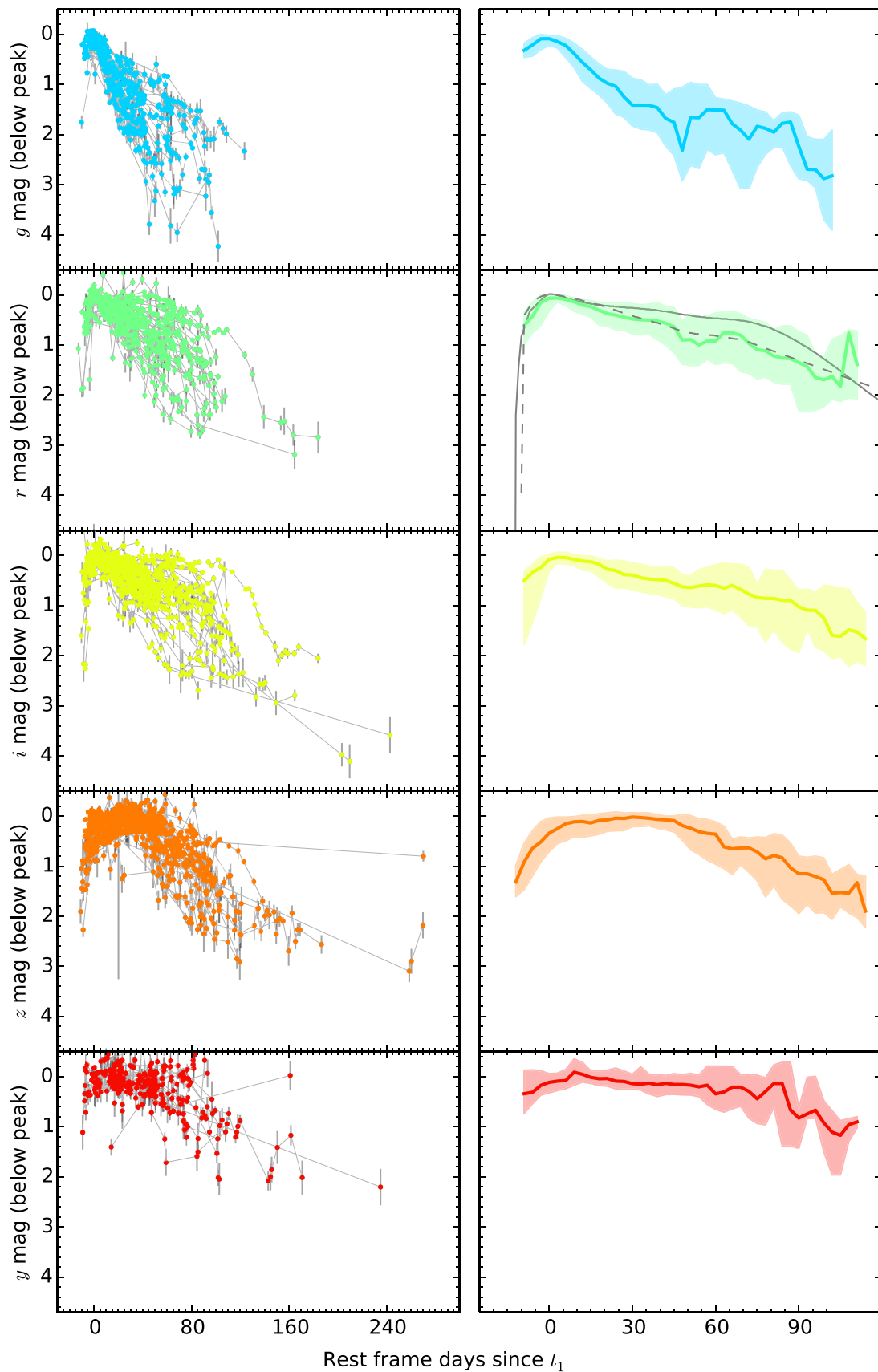
Figure 10. Left: stacked SN IIP light curve constructed from objects in the PS1 sample. The magnitudes are shown relative to the fitted value of M_{peak} (see Section 3.1). Right: template light curves derived from the stacks, zoomed in relative to the stacked light curves. The solid line shows the median value of stacked photometry at each reference epoch, and the shaded region shows the 1σ (16th–84th percentile) range. The gray lines displayed against the r-band curve show the unfiltered SN IIP (solid line) and IIL (dashed line) templates from Li et al. (2011). K-corrections have been applied using the method described in Section 2.3, including uncertainties accounting for the range of epochs allowed for each photometric point by the model fit.

Table 3
SN IIP *grizy* Template Light Curves

Epoch	g	r	i	z	y
−15	...	...	...	...	...
−12	...	...	...	$1.32^{+0.29}_{-0.33}$	...
−9	$0.32^{+0.14}_{-0.14}$	$0.61^{+0.38}_{-0.26}$	$0.50^{+1.28}_{-0.19}$	$0.88^{+0.59}_{-0.34}$	$0.26^{+0.43}_{-0.38}$
−6	$0.21^{+0.22}_{-0.14}$	$0.43^{+0.33}_{-0.29}$	$0.34^{+1.00}_{-0.16}$	$0.65^{+0.55}_{-0.35}$	$0.31^{+0.23}_{-0.45}$
−3	$0.09^{+0.22}_{-0.09}$	$0.15^{+0.46}_{-0.15}$	$0.25^{+0.60}_{-0.22}$	$0.51^{+0.38}_{-0.40}$	$0.18^{+0.20}_{-0.29}$

Notes. The reported epoch is in rest-frame days since peak. The *grizy* photometry is reported in terms of magnitude below peak; the ranges reflect the 16th–84th percentile variation in observed light-curve behavior.

(This table is available in its entirety in machine-readable form.)

### 4.1. SN IIP Light-curve Template

We construct *grizy* SN IIP template light curves based on scaled stacks of our PS1 photometric sample. Figure 10 (left) shows these stacked SN light curves. In each band, we only include objects with a 1σ uncertainty in the peak magnitude of <0.5 mag and with an uncertainty in the plateau epoch of <10 days, as estimated from the marginal posterior of the fitted light-curve model. In total, we include [63, 66, 64, 63, 32] objects in the [g, r, i, z, y]-band templates.

Figure 10 (right) shows the template light curves constructed from these data. The template magnitudes are calculated based on the range of observed photometry within a moving window of 6 rest-frame days in width, between ∼−10 and 110 days from peak magnitude. Template values are only reported if at least four photometric observations fall in the window. In total, we include [434, 586, 760, 757, 267] observations in constructing the [g, r, i, z, y]-band templates. The templates are reproduced in Table 3.

4.2. Search for an SN IIL Subpopulation

Past studies have varied widely in their interpretation of a putative, fast-declining subclass of SNe II commonly labeled "SNe IIL." The SN IIL classification was coined by Barbon et al. (1979), in recognition of a set of six SNe II with an unusually fast decline rate of ∼0.05 mag day^{-1} in the *B* band, constituting ∼26% of their SN II sample. From a theoretical perspective, a fast-declining SN II suggests a less massive H envelope and consequently less sustained power contribution from H recombination. Likely explanations for diversity in H envelope mass among SN II progenitors include variation in progenitor initial mass, with SNe IIL likely to arise from either progenitors with intrinsically less massive envelopes (e.g., initial masses of ∼7–10 $M_\odot$; Swartz et al. 1991) or more massive stars that have been stripped by strong radiation-driven winds (≳18 $M_\odot$; Smith et al. 2011), and/or stars that have been partially stripped by interaction with binary companions (Nomoto et al. 1995).

Observationally, no widely adopted criteria for SN IIL classification have emerged. Patat et al. (1994) divided their SN II light curve set into "linear" and "plateau" classes based on the Barbon et al. (1979) criterion, but they describe the decline rate distribution of these objects as continuous and find no statistical evidence for two modes in the distribution. In their population study of the LOSS SNe, Li et al. (2011) define SNe IIL as having SN IIP-like spectroscopic features, but exhibiting an *R*-band decline of >0.5 mag after explosion. By their selected criterion, they identify seven unambiguous SNe IIL among 81 SNe II, and they determine SNe IIL to represent 10% of the volume-limited
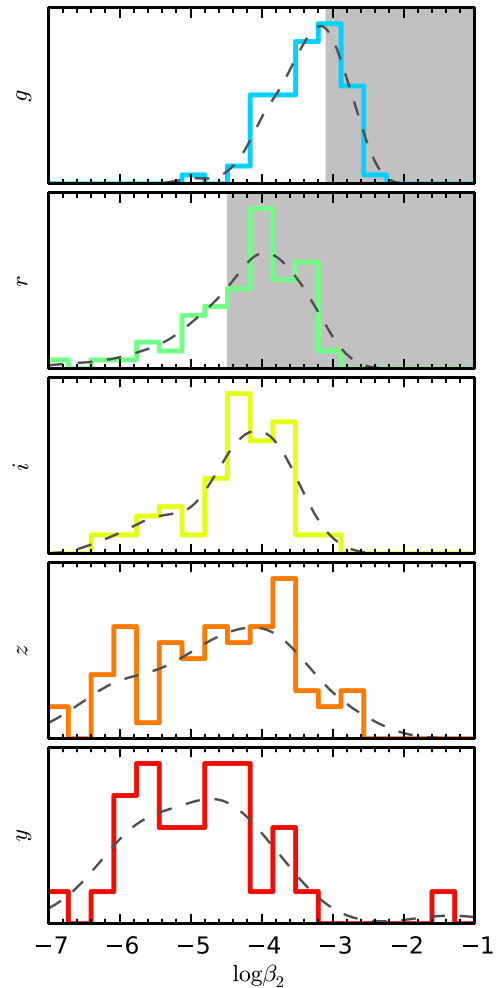
Figure 11. Investigation of a potential SN IIL subpopulation. The histograms display the distribution of mean posterior values for the β_2 plateau decline rate parameter in our fitted light-curve models in each photometric band. Only objects classified nominally as SNe IIP (i.e., not classified as SNe IIn or IIb; see Section 3.4) and only objects with well-constrained β_2 posteriors (with variance ⩽80% of the prior variance) are included. The dashed lines display the Gaussian kernel density estimate models for the distributions. The *g*-band shaded region shows the approximate range for objects that would be classified as SNe IIL under the Barbon et al. (1979) *B*-band criterion (with more positive β_2 values reflecting faster decline rates), and the *r*-band shaded region shows the Li et al. (2011) *R*-band criterion.

SN II population. They find that the SNe IIL are on average overluminous compared to SNe IIP and therefore would represent ∼25% of a magnitude-limited SN II survey sample. By inspection of a set of 22 SN II light curves from the Caltech Core-Collapse Project and the literature, Arcavi et al. (2012) identify a set of five objects that they describe as SNe IIL. Their selection corresponds to a decline rate criterion of ≳0.3 mag within 50 days of explosion. They suggest that these objects form a class "distinct" from SNe IIP and that the two classes together do not form a continuum of decline rates. Most recently, Anderson et al. (2014) have characterized the decline rate distribution of hydrogen-rich SNe as continuous.

We take an empirical approach to searching for evidence of a fast-declining mode in the sample of PS1 objects classified nominally as SNe IIP (see Section 3.4). Figure 11 shows the distribution of mean posterior values for the β_2 plateau decline rate parameter in our fitted light-curve models, among objects with significant constraints on the plateau phase decay

behavior. We employ Gaussian kernel density estimation (KDE) to estimate the underlying form of the decline rate distribution from the observed data. We select a KDE bandwidth factor of 0.43 in r band (and similar in other bands) based on the number of objects in the well-constrained sample, following Scott (1992). Inspection of the KDE models in Figure 11 does not indicate the presence of any fast-declining modes, e.g., within the shaded regions corresponding to the Barbon et al. (1979) and Li et al. (2011) criteria. Given the limited sample size, this test would not be sensitive to the existence of a small SN IIL subpopulation if they are subsumed within the fast-declining tail of a more numerous SN IIP population. However, a significant subpopulation ($\sim$20%), as proposed by previous authors, should emerge if present.

We therefore conclude that empirical evidence for a distinct SN IIL subpopulation is not present within the PS1 SN II data set, and hereafter we do not distinguish between SNe IIL and IIP. Discounting the existence of an SN IIL subclass differs from the interpretation applied in many past studies but does not disagree quantitatively with past results. Li et al. (2011) adopted an SN IIL classification scheme defined arbitrarily by previous authors (Barbon et al. 1979) for the purpose of estimating volumetric rates. Patat et al. (1994) applied a similar criterion and then tested for a discontinuity between the properties of this subpopulation and the "normal" SN IIP population. They reported a negative result. Arcavi et al. (2012) identified a slow-declining subset of objects in their sample but did not quantitatively test for a discontinuity. Moreover, we note that our sample, consisting of 112 SNe II in total, is $\sim$40% larger than the Li et al. (2011) SN II sample and $\sim$5 times larger than the Arcavi et al. (2012) sample. Using a similarly sized sample, Anderson et al. (2014) have reported independent results in agreement with the continuum of decline rates we report here.

Figure 10 further illustrates this result, showing our SN IIP r-band photometry in comparison with the averaged unfiltered SN IIP and SN IIL light curves of Li et al. (2011). Both their templates fall within the photometric range of our observed sample, with their SN IIP template falling near the $+1\sigma$ range of our light curves and their SN IIL template falling near the median of our light curves. Note that their photometry was collected with an unfiltered photometric system, which Li et al. (2011) compare to R band. This would suggest that their response function includes redder wavelengths than our r-band photometry. This may partially explain the slower decline rates in their sample, as redder filters (e.g., izy-bands) exhibit more gradual SN IIP decline rates in the plateau phase. Regardless, this comparison illustrates that the long-recognized range of decline rates among SNe with broad Hα features falls within the observed, continuous range of decline behavior exhibited by objects classified as SNe IIP in our sample, with no evidence for a second, fast-declining mode in the population.

4.3. Plateau Duration Distribution

Recent observational studies have suggested that the plateau durations of SNe IIP are tightly distributed around $\sim$100 days (Poznanski et al. 2009; Arcavi et al. 2012), in stark contrast to theoretical predictions that they should vary from $\sim$80 to 200 days given the expected range of progenitor properties, including mass, energy, and radius (see, e.g., Kasen & Woosley 2009). Poznanski (2013) has interpreted this as evidence that the joint parameter space of progenitor properties must be tightly constrained, with the explosion energy scaling precisely with the cube of the mass to produce a roughly constant plateau duration.
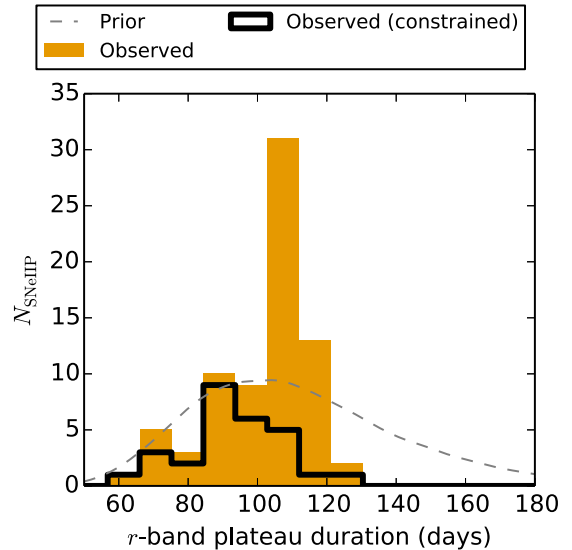

Figure 12. Distribution of r-band plateau durations ($t_p + t_2$) among the SNe IIP in our sample, as derived from the posterior medians of our Bayesian light-curve fits. The solid line shows the subset of objects with well-constrained marginalized posterior uncertainties (<15 days at 1σ; $N = 29$). The dashed line shows the lognormal mixture prior on the plateau duration.

We quantitatively assess the plateau duration distribution of our SN IIP sample. In agreement with Arcavi et al. (2012), Poznanski (2013), and Faran et al. (2014), the r-band plateau duration distribution of our sample (Figure 12) is peaked around $\sim$90–100 days, with median value of 92 days and 1σ variation of 14 days. However, the full observed range of plateau durations is significantly larger, 42–126 days. Note that we do not include in this distribution poorly constrained light curves, where the marginalized posterior uncertainty is $>$80% of the prior variance (24 days at 1σ). For those poorly constrained objects, as Figure 12 illustrates, the posterior is typically peaked around the mean of the prior distribution.

Our PS1 sample therefore suggests that the observed variation in SN IIP plateau durations is not as highly constrained as suggested by Poznanski et al. (2009) and Arcavi et al. (2012). However, we do not detect objects with plateaus as long-lived as the least energetic objects produced in the model grid of Kasen & Woosley (2009) (e.g., $\sim$200 days for kinetic explosion energy of $0.3B$ at infinity). However, all wide-field surveys will be insensitive to identifying the longest-duration objects for two primary reasons. First, such low-energy explosions will have correspondingly low luminosities ($L_{50} \sim 41.8$, similar to the least luminous objects in our sample; see Table 5) and therefore be subject to Malmquist bias. Second, because the lengths of the observing seasons of each PS1 MD field (typically $\lesssim$160 days) are similar to the SN IIP plateau duration, there will be an observational bias toward measuring well-constrained plateau durations only for short-duration objects. We therefore interpret the results presented here as a lower limit on the true variation in the SN IIP plateau duration distribution. In a companion paper, Sanders et al. (2014), we use a hierarchical Bayesian light-curve fitting methodology to assess the influence of these biases on our inferred plateau duration distribution and to estimate the underlying plateau duration distribution.

4.4. Line-of-sight Extinction

We correct for total extinction (Galactic and host environment) using the $(V - I)$ color excess method of Nugent et al.
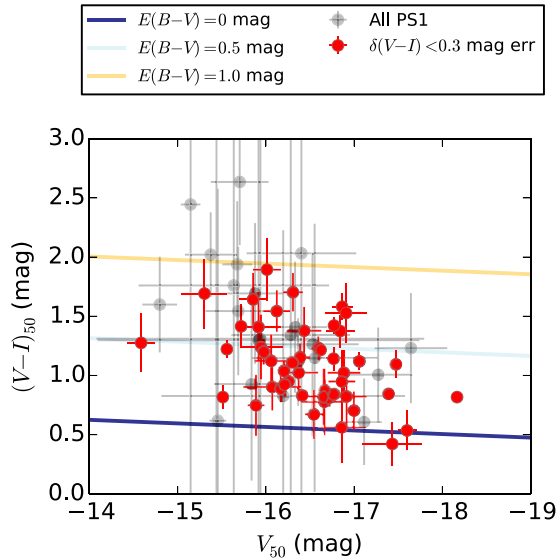
Figure 13. Illustration of $(V - I)$ color excess method for extinction estimation. The points show the V magnitude and $(V - I)$ color (in the Vega magnitude system) at 50 days for objects from our SN IIP sample, with error bars representing 1σ variation in the posterior predictive luminosity distribution for each object. Objects with strong posterior color constraints are highlighted in red. The solid lines show theoretical color–magnitude relations for SNe IIP with different levels of reddening, based on the fiducial relation of Kasen & Woosley (2009).

(2006) as revised by Kasen & Woosley (2009)—see Figure 13. We calculate $E(V - I)$ by comparing with the theoretical baseline $(V - I)$ color[19] for the given V-band luminosity (Equation (15) of Kasen & Woosley 2009) and convert to extinction in each $griz$ band using the extinction curve of Cardelli et al. (1989) and assuming $R_V = 3.1$. We apply a physically motivated uniform prior enforcing $E(V - I) \geqslant 0$ mag. The median uncertainty for the extinction estimate of an individual SN is 0.4 mag.

We find extinctions varying from 0.0 to 4.8 mag, with a median value of $\langle A_V \rangle = 1.3$ mag. In this distribution we have excluded objects with extinction uncertainties $\geqslant 2$ mag, affecting 8 objects. This median is somewhat higher than the mean extinction reported by Smartt et al. (2009) for their sample of SNe IIP with progenitor imaging, $\langle A_V \rangle = 0.7 \pm 1.1$ mag. The discrepancy may result from a combination of differences in methodology (the estimates from Smartt et al. 2009 are derived from a heterogeneous set of sources and techniques) and sample selection (given that our PS1 transient search operates in red bands, particularly i and z, it may be relatively insensitive to selection against high-extinction objects). Both observations and theory show that there is significant scatter around the fiducial $(V - I)$ color, indicating intrinsic color variation not accounted for in our color-excess-based extinction estimate. Moreover, the color excess method may be particularly vulnerable to underestimates for low-metallicity progenitors where decreased iron line blanketing would reduce suppression of blue flux. We note that Faran et al. (2014) have recently shown

---

[19] We convert our $griz$ photometry to the Landolt and Vega systems using a color-based S correction obtained by integrating over the temporally nearest available UV–optical–IR spectrum of SN 1999em, the $\sim{+}37$ day spectrum from Leonard et al. (2002). We find that s-corrections based on the spectrophotometric templates applied in Section 2.3 would introduce a systematic discrepancy in the $(I - i)$ color relative to SN IIP corrections in past works (e.g., D'Andrea et al. 2010) of $\sim$0.4 mag, owing to differences in the equivalent width of the near-IR Ca II emission feature. We estimate that a $\sim$0.1 mag systematic uncertainty may remain in our I-band magnitude estimates owing to variation in this feature. We apply the AB offset of Blanton & Roweis (2007).

Table 4
SN IIP Absolute Magnitude Distribution Statistics

F		Observed				Extinction Corrected		
	N	16th	50th	84th	N	16th	50th	84th
g	36	−16.86	−17.86	−18.43	13	−17.84	−19.14	−19.70
r	50	−16.92	−17.80	−18.45	23	−17.47	−18.10	−19.28
i	49	−17.08	−17.68	−18.33	26	−17.31	−18.10	−18.94
z	40	−17.11	−17.89	−18.42	33	−17.63	−18.06	−19.25

Notes. The [16, 50, 84]th columns correspond to percentile values within the SN IIP absolute, K-corrected peak magnitude distribution, without ("observed") and with extinction correction (Section 4.4). Only PS1 SNe IIP with low posterior uncertainty in their peak magnitudes are included ($\delta M < 0.1$ mag at 1σ without extinction correction, $\delta M < 0.2$ mag with); the total number of objects in each distribution (N) is given. Each row corresponds to a PS1 photometric filter (F).

that both photometric and spectroscopic SN IIP extinction correction prescriptions have limited effectiveness (as measured by their ability to reduce the scatter in observed colors) and exhibit systematic offsets relative to each other.

4.5. Peak Magnitude Distribution

We show the peak absolute magnitude distribution for our PS1 SN IIP sample in each photometric filter in Figure 14. We correct for extinction using the $(V - I)$ color excess method, as described in Section 4.4. Statistics of these distributions are given in Table 4. In this table and hereafter, we include only objects with well-constrained posterior distributions: $\delta M_{\rm peak} < 0.1$ mag at 1σ without extinction correction, and $\delta M_{\rm peak} < 0.2$ mag with correction. The median uncertainty for the absolute magnitude measurement (1σ posterior width) is $\delta M_{\rm peak}$ of 0.07 mag in r band without extinction correction, and 0.35 mag after correction.

The observed peak magnitude distribution agrees well with the R-band luminosity function of Li et al. (2011), reflected in the prior distribution shown in Figure 14 (see also Section 3.2 and Figure 6). The comparison is somewhat limited, as Li et al. (2011) examined a different filter (R) and did not correct for extinction (although the objects in their sample should have low extinction). Note that this similarity suggests agreement of the observed distribution of peak magnitudes between our surveys. If the prior were simply dominating our inferred peak magnitudes, the posterior medians would all be centered at the prior mean ($M_{\rm peak} = -17.5$). This effect can be seen in the y-band peak magnitude distribution shown in Figure 14, where prior information does dominate for a substantial fraction of objects. Extinction correction shifts the median of the distribution by $\sim$0.6 mag in g band and only by $\sim$0.1 mag in z band. We regard the y-band distribution as least reliable owing to the small number of objects ($N = 15$) that pass our posterior width cut, and therefore we do not include them in Table 4.

The extinction-corrected peak magnitude distribution spans a 1σ range of -17.47––-19.28 mag in r band, indicating a factor of $\sim$3 spread in the luminosity distribution of these SNe. This wide range in SN properties has important implications for the mass distribution of their progenitor stars, which we model and discuss in Section 5.4. Richardson et al. (2014) found a B-band volume-limited peak magnitude distribution with mean and standard deviation of $M_B \sim -17 \pm 1$ among 74 SNe IIP from the literature, $\sim$1.5 mag dimmer than the
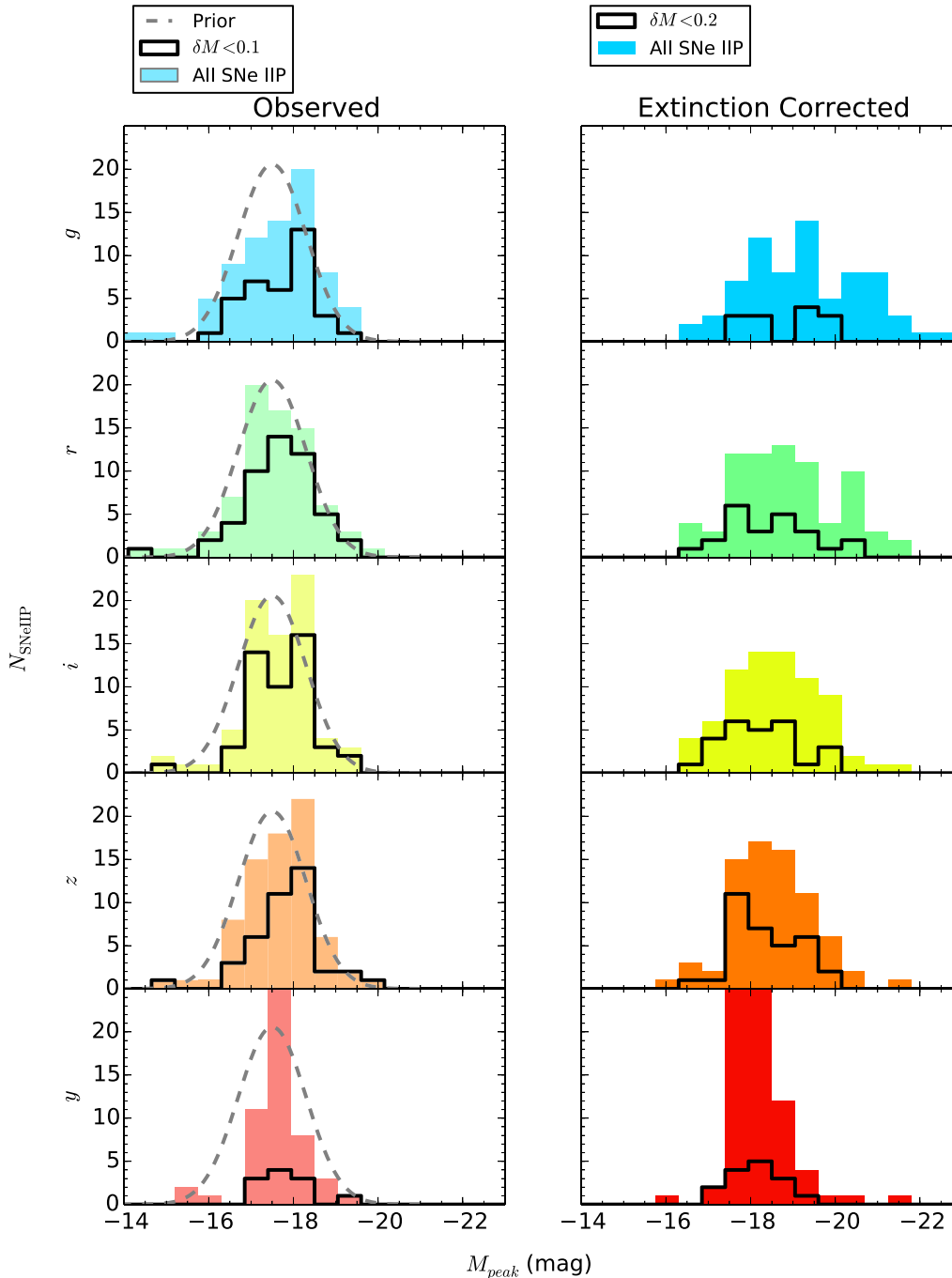
Figure 14. Peak absolute magnitude distribution among the SNe IIP in our PS1 sample, as derived from the posterior medians of our Bayesian light-curve fits, without (left) and with (right) correction for extinction (see Section 4.4). The solid line shows the subset of objects with well-constrained marginalized posteriors (<0.1 mag at 1σ without extinction correction, <0.2 mag with correction). The dashed line shows the prior distribution discussed in Section 3.2. All data are K-corrected.

g-band mean peak magnitude we report. The discrepancy in the mean of the absolute magnitude distributions between our study and theirs is likely due to a combination of sample selection effects and extinction correction methodology. Richardson et al. (2014) have considered SNe IIL separately from SNe IIP, which systematically lowers their SN IIP peak magnitude distribution relative to ours (see Section 4.2). Moreover, Richardson et al. (2014) have applied a statistical correction for extinction, assuming a mean value of $A_B \sim 0.3$ mag for each CCSN, which is typically ~1 mag lower than the extinction correction we measure among our SNe IIP with the $(V - I)$ color excess method (Section 4.4).

4.6. Decline Rate–Peak Magnitude Relation

Upon investigation of the joint posterior parameter distributions among our fitted SN IIP light curves, we identified a highly significant relation between the plateau phase decline rate (β_2) and the extinction-corrected peak magnitude (M_{peak}) of the SNe. Figure 15 illustrates that these parameters are highly correlated in r band, with Pearson correlation coefficient of -0.50 (p-value of 5×10^{-06}). We have evaluated the strength of the correlation between these parameters in all combinations of photometric filters available from the PS1 data set (Figure 16) and identified this relation to be significant in every band (except y, where the

14
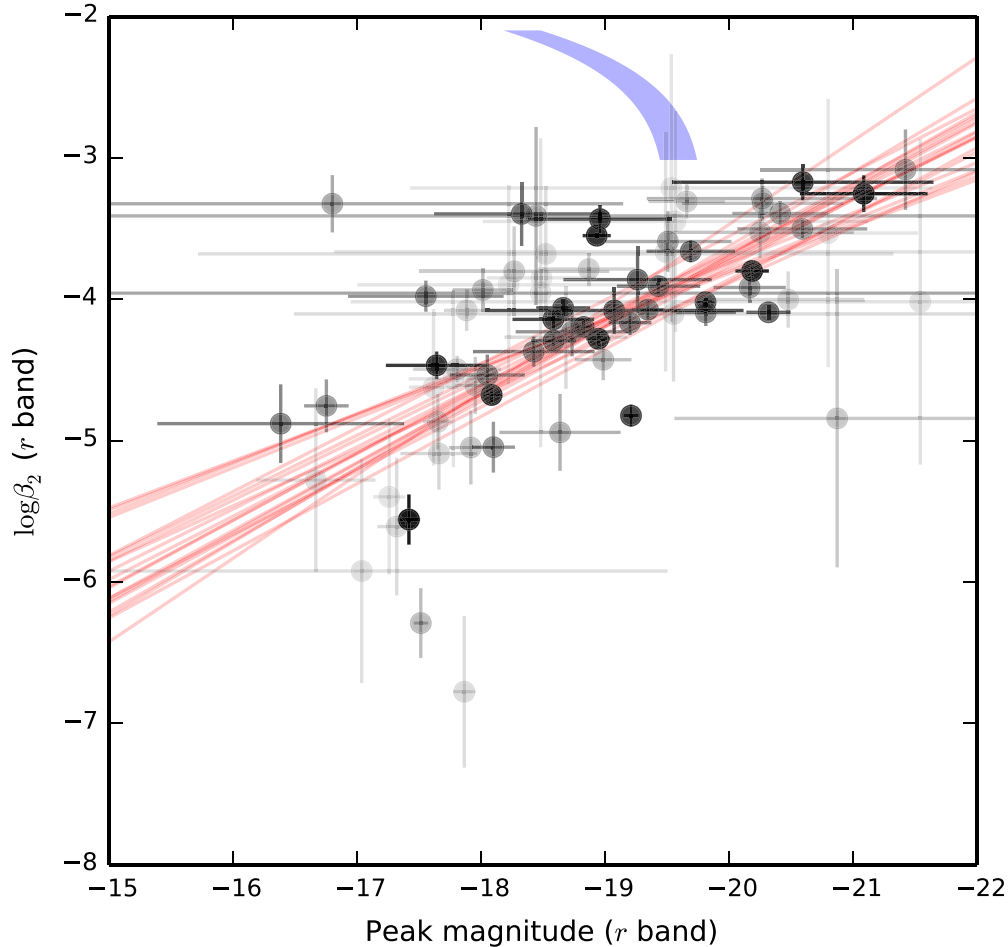
Figure 15. Relation between the plateau phase decay rate (β_2, r-band) and the extinction-corrected r-band peak magnitude (M_{peak}) among SNe IIP in the PS1 sample. The red lines show posterior samples of linear fits to the parameter values. The opacity of the points is drawn in proportion to the inverse of their posterior variance. The blue band shows the SN Ia width–luminosity relation of Phillips et al. (1999), assuming $M_r^{\mathrm{max},Ia} = -19.45$ mag and a dispersion of 0.15 mag.

PS1 photometry is limited), though it is strongest in the r and i bands.

In the r band, the relation between these parameters is best fit with the relation

$$\log \beta_2[r] = (-13.1 \pm 1.2) + M_{\mathrm{peak}}[r](-0.47 \pm 0.07). \quad (6)$$

This linear fit was obtained using a Bayesian methodology accounting for the two-dimensional covariance of the M_{peak} and β_2 posterior distributions for each SN and modeling the relationship between these values with an intrinsic scatter V orthogonal to the axis of the fit line (Hogg et al. 2010). The [16, 50, 84]th percentile values of the intrinsic scatter parameter, projected to the peak magnitude axis, are [0.14, 0.16, 0.19] mag. No samples among the 20,000 returned from our MCMC fit of this model have positive slopes for the linear fit, supporting the low p-value reported from the Pearson correlation coefficient test above. When we perform the same analysis on the observed absolute peak magnitudes, not corrected for extinction, we find a similar trend, but with somewhat decreased significance (p-value of 1×10^{-05} and projected intrinsic scatter median $V = 0.26$ mag). This result suggests that application of the color-excess-based extinction estimates provides measurable success in recovering the intrinsic distribution of light-curve properties, despite the shortcomings described in Section 4.4. Considering the V-band data of Anderson et al.

(2014)[20] and applying the same Bayesian linear fitting methodology yields a median intrinsic scatter of $V = 0.3$ mag. The larger intrinsic scatter indicated by the Anderson et al. (2014) data results in part from the much smaller uncertainties in the light-curve parameters of the nearby SNe they study. This discrepancy may imply that the uncertainties in our light-curve parameters are somewhat overestimated, or that theirs are somewhat underestimated.

In past studies, divisions of SN IIP samples into "normal" SN IIP and SN IIL (see Section 4.2) subclasses may have obscured this relation by reducing the dynamic range available for correlations against the decline rate. Anderson et al. (2014) have recently reported an independent discovery of this relation using a similarly sized sample of V-band light curves from a variety of past SN searches. This independent discovery, as well as the multiband manifestation of the relation that we explore here, underscores its physical significance. This result echoes past conclusions that "SNe IIL" are on average more luminous than more slowly declining SNe IIP (e.g., Patat et al. 1994; Li et al. 2011).

The existence of a decline rate–peak magnitude relation for SNe IIP is reminiscent of the well-known width–luminosity relation for SNe Ia (e.g., Phillips et al. 1999). However, while

---

[20] Here we exclude SN 2008bp, which Anderson et al. (2014) identify as an outlier and special case, and we transform their s_2 parameters to our β_2 given that $\log \beta_2 = \log(s_2/108.6)$.

Table 5
Light Curve and Modeled Progenitor Parameters for PS1 SNe IIP

PS1 SN	$M_{p,r}$ (mag)	$t_{\mathrm{plateau},r}$ (days)	$\log_{10}(L_{50})$ (erg s^{-1})	$\Delta m_{15,r}$ (mag)	M_{Ni} (mag)	M_{in} ($M_\odot$)	R_0 ($R_\odot$)	E_{51} (10^{51} erg)
PS1–10a	$-18.11^{+0.17}_{-0.20}$	114^{+32}_{-30}	$42.63^{+0.55}_{-0.41}$	$-0.52^{+0.28}_{-0.38}$	$0.15^{+0.32}_{-0.11}$	. . .	. . .	. . .
PS1–10q	$-17.06^{+0.04}_{-0.05}$	96^{+4}_{-2}	$42.42^{+0.15}_{-0.12}$	$-0.26^{+0.02}_{-0.02}$	$0.11^{+0.19}_{-0.07}$	. . .	. . .	. . .
PS1–10ae	$-17.17^{+0.04}_{-0.04}$	112^{+28}_{-26}	$41.93^{+0.20}_{-0.13}$	$-0.30^{+0.03}_{-0.04}$	$0.06^{+0.07}_{-0.04}$	. . .	. . .	. . .
PS1–10lv	$-18.43^{+0.04}_{-0.03}$	109^{+21}_{-7}	$43.12^{+0.04}_{-0.06}$	$-0.27^{+0.01}_{-0.01}$	$0.20^{+0.14}_{-0.14}$	. . .	. . .	. . .
PS1–10mb	$-15.46^{+0.15}_{-0.17}$	103^{+27}_{-20}	$41.80^{+0.20}_{-0.15}$	$-0.08^{+0.04}_{-0.05}$	$0.06^{+0.06}_{-0.04}$	. . .	. . .	. . .

Notes. The r-band peak magnitude ($M_{p,r}$) is derived directly from the model fits (Section 3.2), including K-corrections, but not corrected for extinction. The r-band plateau duration ($t_{\mathrm{plateau},r}$) is in rest-frame days, not corrected for contamination by ^{56}Ni. The pseudobolometric (optical–IR) luminosity at 50 days (L_{50}) is measured from the fits to the PS1 photometry; the value quoted does not include the bolometric correction described in Section 3.2. The decline rate in r band ($\Delta m_{15,r}$; rest-frame days) is measured from the same model fits. The ejected nickel mass is estimated from comparison of the late-time bolometric light curve with that of SN 1987A (but see Section 5.2 for a discussion of reliability). The progenitor initial mass (M_{in}), radius (R_0), and explosion energy (E_{51}) estimates come from the comparisons (see Section 5.3) with the models of Kasen & Woosley (2009); but see Section 5.4 for a discussion of reliability. These theoretical estimates are reported only if the central mass estimate falls within the model grid (12–25 $M_\odot$), but the full posterior distribution for the reported values includes extrapolations to values beyond the model grid, as reflected in the reported uncertainties. All reported values represent [16,50,84]th percentiles of the posterior distribution.

(This table is available in its entirety in machine-readable form.)
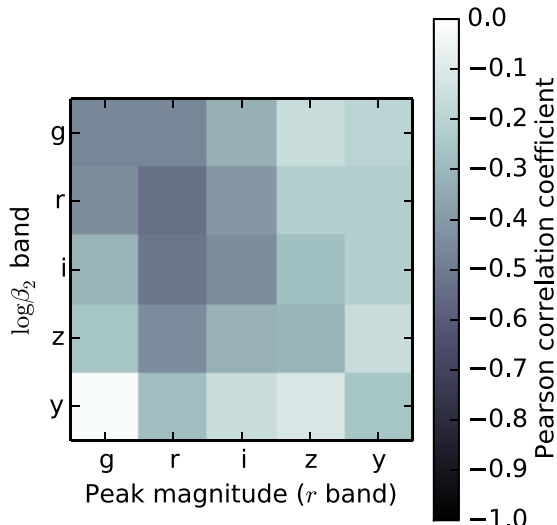
Figure 16. Comparison of $\beta_2 - M_{\mathrm{peak}}$ (extinction-corrected) relation for different photometric filter sets. The shading represents the strength of the correlation between the two variables in each pair of photometric filters, as measured by the Pearson correlation coefficient (key at right).

brighter SNe Ia have more slowly declining light curves, brighter SNe IIP instead have faster-declining light curves (Figure 15). Moreover, the SN IIP relation has significant intrinsic scatter: $V \sim 0.2$ mag. That the SN IIP decline rate–peak magnitude relation is recoverable at all is testament to the wide range of variation in their plateau phase decline rates, which ranges a factor of ~ 20.

The SN Ia decline rate–peak magnitude relation is interpreted as evidence for a fundamental plane or single-parameter family among SN Ia light curves, and a similarly sparse dimensionality may apply to SNe IIP. Several authors have argued for a single parameter source of variation among SN IIP light curves (Hamuy 2003; Poznanski 2013), particularly with respect to the luminosity–velocity relation applied in the standardizable candle method (Hamuy & Pinto 2002; Olivares 2008; D'Andrea et al. 2010). Interpreted together with the results of Section 4.2, this would seem to point to the explosion energy, likely determined by the progenitor initial mass through its influence on

the mass of the hydrogen envelope at the time of explosion, as the predominant single parameter continuously determining the fundamental observational properties of the explosions of hydrogen-rich red supergiants, as Anderson et al. (2014) also concluded. However, the presence of significant scatter around the SN IIP decline rate–peak magnitude relation presented here suggests additional correlations with secondary factors, as have emerged among SNe Ia (Wang et al. 2009; Foley et al. 2011). Relevant secondary characteristics of the progenitor stars are likely to include metallicity and rotation velocity.

In general, more massive H-rich envelopes should have longer radiative diffusion times ($t_{\mathrm{diff}} \propto M/R$), suggesting slower light-curve evolution and lower peak magnitudes. However, Poznanski (2013) have found an empirical linear relation between the progenitor initial mass of SNe IIP and their expansion velocities in the plateau phase. With these two factors in opposition, this would suggest that the diffusion time, and perhaps the β_2 parameter, should be nearly constant among SNe IIP. This discrepancy could result from nonlinearity in the relationship between progenitor initial mass and the mass of the hydrogen envelope at the time of explosion or variation in the velocity evolution between SNe IIP. Alternatively, it may challenge the robustness of the linear mass–velocity relation constructed by Poznanski (2013).

5. PROGENITOR MODELING

We compare the light-curve models for each SN IIP in our sample to relevant theoretical models to estimate the physical properties of their progenitor stars.

5.1. Bolometric Luminosity

For the purpose of comparing with the full-wavelength spectrophotometric models of Kasen & Woosley (2009), we estimate the pseudobolometric (optical–IR) luminosity of each SN by integrating over the multiband ($grizy$) light-curve model described in Section 3.2. We apply a correction to the pseudobolometric light curves to, primarily, account for unobserved IR flux and some UV emission. We calculate this correction (pBC) by integrating an SN IIP spectral template from a similar epoch ($t = +61$ days; Gilliland et al. 1999; Baron et al. 2004) over the $'griz'$ bands, obtaining pBC $= 0.38$ mag. By
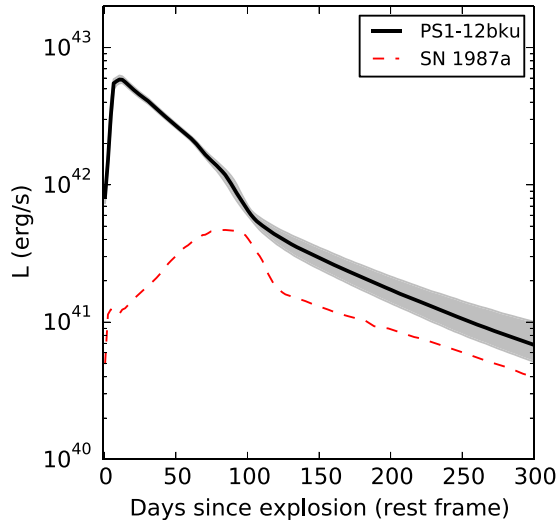
Figure 17. Illustration of ejected nickel mass (M_{Ni}) measurement methodology. The pseudobolometric (optical–infrared) light curve for PS1-12bku (black solid line) is shown in comparison with the late-time bolometric light curve of SN 1987A (red dashed line; from Pastorello et al. 2004, and references therein). The 1σ uncertainty in the bolometric luminosity as derived from the multiband light-curve model is illustrated with the shaded region, including the uncertainty in the explosion epoch.

using a fixed spectral template, we neglect any intrinsic variation in the SN IIP spectral properties. The modeling in Kasen & Woosley (2009) suggests that any intrinsic color variation among SNe IIP is small, with the bolometric correction estimated to vary by ~ 0.1 mag based on differences in progenitor metallicity and initial mass (their Figure 14).

5.2. Ejected Ni Mass

We estimate the ejected mass of radioactive ^{56}Ni (M_{Ni}) by comparison to the late-time light curve of SN 1987A (see Figure 17), following the method of Pastorello et al. (2004). We compare our pseudobolometric light curves (Section 5.1) with the SN 1987A light curve using the late-time (>125 days) rest-frame epoch where the model is most tightly constrained and assuming complete gamma-ray trapping, as in Pastorello et al. (2004); but see also the discussion of gamma-ray trapping in Anderson et al. (2014).

The distribution of M_{Ni} among our PS1 SNe IIP has [16, 50, 84]th percentile values of [0.04, 0.12, 0.20] $M_\odot$ (see Figure 18). We include in this distribution only objects with photometry to directly constrain their light-curve evolution in the radioactive-decay-dominated phase. We identify such objects by looking at the posterior variance in the β_{dN} parameter, which is $\delta\beta_{dN} = 1$ dex at 1σ in cases where the prior alone sets the parameter value. We therefore adopt a cut at $\delta\beta_{dN} < 0.9$ dex to exclude poorly constrained Ni masses. We note that, among the entire sample, the typical uncertainty in M_{Ni} is fairly large (median of 0.4 dex) owing to the relatively poor photometric coverage of the late phases of SNe in the sample. Among the excluded objects, some have unphysically large median estimates for the ejected ^{56}Ni mass ($M_{Ni} > 1\ M_\odot$); the high uncertainty in these estimates is appropriately reflected in the confidence intervals quoted in Table 5.

Our results suggest a factor of ~ 2 smaller M_{Ni} for most SNe IIP in comparison with typical SNe Ib and Ic, which have $\langle M_{Ni}\rangle \approx 0.20 \pm 0.16\ M_\odot$ (Drout et al. 2011). This is consistent with the expectation that SNe Ib and Ic are produced by more
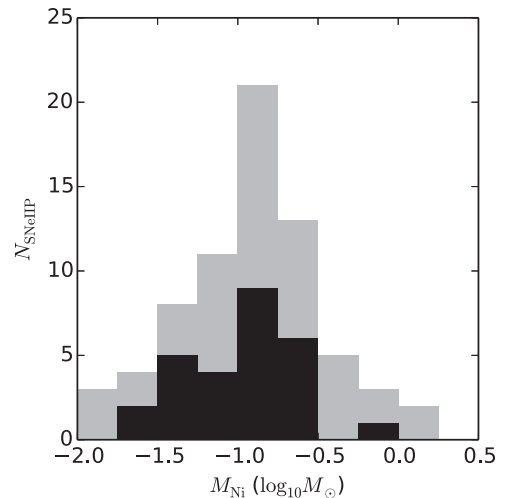
Figure 18. Distribution of ejected nickel mass (M_{Ni}) among the SNe IIP in our sample, as derived from the late-time bolometric luminosity. The gray shaded area shows the distribution estimated among all objects in our sample, and the black shaded region shows only objects with photometry constraining the light-curve evolution in the radioactive decay phase (based on the variance in the β_{dC} posterior; see the text).

massive stellar progenitors than SNe IIP. Our measured M_{Ni} distribution is similar to that reported by Nadyozhin (2003), who derive M_{Ni} ranging from 0.03 to 0.4 $M_\odot$ for a set of 11 SNe IIP from the literature, with a mean value of 0.10 $M_\odot$.
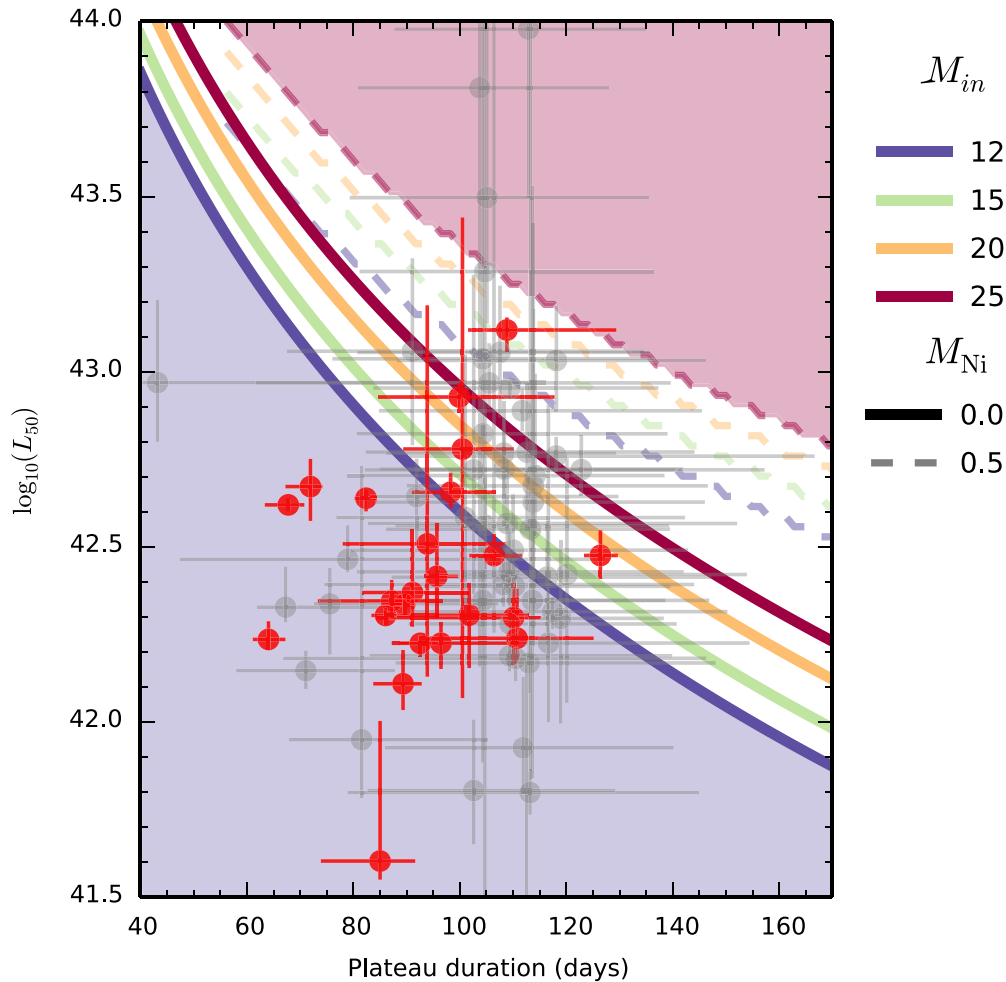
5.3. Comparison to Hydrodynamic Models

We derive physical parameters (including progenitor initial mass, radius, and explosion energy) for the progenitor stars of our SN IIP sample by comparison with the modeling of Kasen & Woosley (2009). In general, more massive progenitor stars produce plateaus that are brighter and of longer duration. There is a secondary contribution from M_{Ni} that has the effect of increasing the plateau duration. Kasen & Woosley (2009) provide scaling relations for the observable parameters L_{50} (bolometric luminosity at 50 days after explosion) and $t_{p,0}$ (plateau phase duration, corrected for extension by ejected ^{56}Ni) as a function of E_{51} (total explosion energy in units of 10^{51} erg) and M_{in} (initial mass of progenitor star). We note that there is a well-known discrepancy between masses derived from hydrodynamic light-curve modeling and direct progenitor searches, with progenitor searches yielding lower mass estimates (Utrobin & Chugai 2008; Maguire et al. 2010).

We derive $t_{p,0}$ using their Equation (13), which requires an estimate for M_{Ni} (see Section 5.2), R_0 (the progenitor radius at the time of explosion), and M_{ej} (the total ejected mass). Following the recommendations of Kasen & Woosley (2009), we calculate values for R_0 and M_{ej} strictly as a function of M_{in} by interpolating over the progenitor star model grid used in their study. Solving this system of equations for every sample in the posterior distribution of the light-curve model, we obtain estimates for M_{in}, M_{ej}, and E_{51} for each SN IIP in our sample.

5.4. Progenitor Initial Mass Inference

In Figure 19 we compare the observed plateau duration and L_{50} with model curves from Kasen & Woosley (2009). This comparison illustrates that the observed variation in SN IIP light-curve phenomenology is significantly larger than the range explored by the Kasen & Woosley (2009) model grid, preventing us from performing progenitor parameter estimation

Figure 19. Comparison of observed SNe IIP light-curve properties with hydrodynamic light-curve models. The points show the plateau duration (t_p+t_2, rest frame; not corrected for M_{Ni}) of SNe IIP from the PS1 sample vs. their bolometric luminosity at 50 days after explosion (L_{50}). Red points have well-constrained values for the plateau duration ($\delta t_p < 20\%$), while gray points have poorer constraints. The solid lines show interpolated values for progenitors of different initial masses (M_{in}; key at right) from the model grid of Kasen & Woosley (2009). Different curves are plotted to illustrate the range of variation with the mass of ejected radioactive nickel ($M_{Ni} = [0, 0.50]\ M_\odot$ for [solid, dashed] line styles, respectively). The shaded curves illustrate physical parameter space not explored by the Kasen & Woosley (2009) model grid, ostensibly corresponding to masses <12 or >25 $M_\odot$.

for a substantial number of the objects in our sample. Given the observed M_{Ni} values measured for each individual light curve, 67 of our SNe IIP have light-curve properties outside the region covered by the Kasen & Woosley (2009) models, and we can produce mathematically valid comparisons with model light curves from the Kasen & Woosley (2009) grid for only 8 SNe IIP (see Table 5). Even these comparisons typically yield explosion energies at or above the most energetic models in their grid ($E_{51} > 5$). A large number of objects in our sample have luminosities lower than the range of theoretical values for a given plateau duration (falling in the blue shaded region of Figure 19), accounting for 61 of the 67 objects for which we do not report progenitor inferences.

We therefore advocate for further theoretical exploration of the SN IIP light-curve parameter phase space through additional hydrodynamic modeling, in order to provide more robust model grids and scaling relations for comparison with observational surveys. In particular, certain modeling systematics should be addressed to enable inference on objects occupying the low-luminosity and short plateau duration parameter space. Dessart & Hillier (2011) have previously recognized a systematic discrepancy between SN IIP model and observed light curves and identified oversized radii in model progenitor stars as the

likely cause. Hydrodynamic explosion simulations based on more advanced progenitor star models, taking into account important effects such as rotation on the stellar radius (e.g., Georgy et al. 2013), are needed to overcome this bias. Moreover, synthetic light curves for SNe with progenitor initial masses <12 $M_\odot$, down to the limit for core collapse (e.g., 8 $M_\odot$; see Smartt et al. 2009, and references therein), and higher explosion energies should be produced. Such low-mass progenitors have already been explored in the context of extremely low luminosity SNe IIP like SN 1997D (Chugai & Utrobin 2000), and model light curves of this kind calculated with full self-consistency across the mass and energy spectrum are needed.

Additionally, other progenitor physical parameters will play important secondary roles in determining SN light-curve properties and should be included in future simulations. In particular, lower metallicity can serve to lower the plateau luminosity by decreasing the opacity of the H envelope, therefore lowering plateau luminosities, and by decreasing mass loss, causing longer-lived H recombination and plateau durations (Kasen & Woosley 2009; Dessart et al. 2013). Dessart et al. (2013) have recently performed a theoretical survey of SN IIP radiative properties using a grid of synthetic progenitor stars expanded in parameter scope with respect to the grid of Kasen & Woosley

(2009), including core overshoot, rotation, mixing, and metallicity. However, the Dessart et al. (2013) grid was limited to a single initial progenitor mass of 15 $M_\odot$. An expanded survey of the kind performed by Dessart et al. (2013), to provide updated observationally applicable scaling relations of the kind provided by Kasen & Woosley (2009), would be an invaluable tool for inference on the progenitor population of massive star explosions in the nascent untargeted survey era. Photometric galaxy metallicity diagnostics like that presented in Sanders et al. (2013) can be used to observationally estimate metallicities for the progenitor stars of observed SNe to facilitate model comparison.

5.5. Implications for the Red Supergiant Problem

While theoretical stellar evolution modeling has historically predicted that stars undergoing core collapse up to ∼25 $M_\odot$ should produce SNe IIP (see, e.g., Eldridge 2008; Smartt 2009, and references therein), a variety of observational techniques have failed to identify SN IIP progenitors with masses greater than ∼16 $M_\odot$. The shape of the stellar initial mass function (IMF) can at least help to explain this absence, with ∼8 $M_\odot$ progenitors being a factor of 10–15 times more common than ∼25 $M_\odot$ progenitors. However, even accounting for IMF prescriptions of varying steepness, Smartt (2009) reported an upper limit for the SN IIP progenitor mass of 16.5 $M_\odot$ based on their direct progenitor detection search. Similarly, in an X-ray analysis of SN IIP progenitor mass-loss rates, Dwarkadas (2014) estimated a maximum mass-loss rate of ∼19 $M_\odot$. Black hole fallback formation (Fryer 1999; Heger et al. 2003) and/or progenitor rotation (Georgy et al. 2013; Groh et al. 2013b) may provide a theoretical solution to this "red supergiant problem."

Our results have only indirect implications for the red supergiant problem. While our progenitor mass estimates (e.g., Figure 19) show no evidence for an absence of SN IIP progenitor stars at the high-mass end of the Kasen & Woosley (2009) progenitor grid, our mass estimates are only as reliable as the calibration of the hydrodynamic modeling underpinning them. As we have discussed, there are known systematic offsets between the masses inferred from hydrodynamic modeling and progenitor star photometry, and additional theoretical investigation of this discrepancy is needed to conclusively resolve the red supergiant problem.

However, our observations and modeling suggest that there is no discontinuous distinction between SNe IIP and IIL (Section 4.2). Given the correlation between plateau phase decline rate and luminosity (Section 4.6) and the theoretical connection between luminosity and progenitor mass, the exclusion of luminous "SNe IIL" could obscure the high-mass end of the SN IIP progenitor population. Emphasizing the role of small number statistics in this regime, we note that Smartt (2009) report a progenitor mass upper limit that is already consistent with 20 $M_\odot$ at 2σ, and consistent with >25 $M_\odot$ at 2σ if only events with robust progenitor detections are included in the analysis. Walmswell & Eldridge (2012) have recently considered the extinction due to the dust produced by red supergiant winds and revised the SN IIP upper mass limit to 20^{+6}_{-3} $M_\odot$ (with 2σ uncertainty). As the direct progenitor search technique has so far only been applied to a handful of objects, we look to future detections of the progenitors of luminous SNe IIP to address the red supergiant problem (see, e.g., Fraser et al. 2010; Elias-Rosa et al. 2011).

6. CONCLUSIONS

We have assembled and studied the full sample of SN IIP light curves from the Pan-STARRS1 Medium Deep Survey, totaling 18,953 photometric data points (5,096 robust transient detections) in *grizy* filters for 112 individual SNe (76 SNe IIP). We have developed a Bayesian light-curve fitting methodology for SNe II based on a physically motivated five-component segmentation of the SN IIP light curve (Section 3.1). We present an implementation of our SN IIP model for use with the Hamiltonian Monte Carlo library *Stan* in Appendix A. We have interpreted our light-curve modeling in terms of the hydrodynamic SN IIP progenitor model grid of Kasen & Woosley (2009).

The primary conclusions of this work are as follows.

1. We present photometric K-corrections and SN IIP light-curve templates in the *grizy* bands (Sections 2.3 and 4.1). Our templates are based on 2,804 individual photometric detections for 66 individual SNe IIP from −15 to +114 days from peak magnitude.

2. Consistent with theoretical expectations, our SN IIP sample spans a diverse range of light-curve parameters: a factor of ∼20 in plateau phase decay rate (Figure 11), ∼2 orders of magnitude in ejected ^{56}Ni (Figure 18), a factor of ∼2 in plateau duration (Figure 12), and ≳4 mag in absolute magnitude (Figure 14). This evidence stands in contrast to recent suggestions by Arcavi et al. (2012) and Poznanski (2013) that the SN IIP plateau duration distribution, a critical observational parameter tied to progenitor initial mass, is tightly distributed (Section 4.3).

3. Addressing a long-standing debate in the literature, we have searched for the existence of a fast-declining "SN IIL" subpopulation in the decline rate distribution of our SN IIP sample (Section 4.2). We find no evidence for a discontinuity in this distribution for any photometric band, questioning the existence of a discrete SN IIL subpopulation.

4. We identify a highly significant statistical correlation between the peak magnitude and plateau phase decline rate of SNe IIP (Section 4.6). Together with the previous results, this supports the interpretation of core collapse among hydrogen-rich red supergiants as a predominantly single-parameter family of explosions, whose observational behavior is determined primarily by the explosion energy and likely set by the initial mass of the progenitor star. This represents an independent discovery and confirmation of results recently reported in Anderson et al. (2014).

5. Through the largest systematic comparison to date of SN IIP light curves with hydrodynamic progenitor models, we have derived mass, radius, and explosion energy estimates for the objects in our sample (Section 5.4). However, we find that the available theoretical model grids are insufficient to cover the full range of observed variation in SN IIP light-curve properties. We point to the need for additional hydrodynamic modeling to produce updated and expanded self-consistent model grids, particularly in the low-luminosity regime.

6. Though our progenitor inferences are based on hydrodynamic light-curve models, which are known to produce systematically higher masses than direct progenitor detection searches, we do not find evidence for an absence of high-mass SN IIP progenitors (Section 5.5). We point to future direct progenitor detections of luminous SNe IIP as having the potential to ease the discrepancy between the

maximum SN IIP progenitor mass identified by various theoretical and observational methods, known as the red supergiant problem.

In a companion paper, Sanders et al. (2014), we discuss and demonstrate a hierarchical expansion of the model presented here to provide a general framework for the analysis of SN light-curve populations in the coming era of next-generation wide-field transient searches. We advocate continued investment in statistical and computational tools in the future as a means to compensate for the relative decline anticipated in the availability of detailed spectroscopic and other follow-up information on individual transients.

APPENDIX A

INDIVIDUAL LIGHT-CURVE *STAN* MODEL

Below we reproduce the full Bayesian model for our five-component segmented SN II light-curve model described in Section 3.2, in the *Stan* modeling language. The Stan model specification format is documented in the Stan Modeling Language Users Guide and Reference Manual (Stan Development Team 2014b).

The model takes the following data as input: N_obs, the total number of photometric data points; N_filt, the number of photometric filters; t, a vector of MJD dates of the photometric observations; fL, a vector of luminosities corresponding to the photometric observations (with units as described in Section 3.1); dfL, a corresponding vector of luminosity uncertainties; z, the redshift; t0_mean, an initial estimate of the explosion date (for initialization and for centering the explosion date prior distribution); J, a vector of integers specifying the filter ID of each photometric observation; Kcor_N, a matrix of precomputed *K*-corrections for each filter, in magnitudes with spacing of 1 day; fluxscale, the zero point of the luminosity unit system ($\texttt{fluxscale} = 10^7$ in the system we have employed); and duringseason, a Boolean value specifying whether the object exploded within or between observing seasons, for selection of the explosion date prior distribution parameters. The calculation of the model light-curve flux and application of the *K*-correction values are performed in the `transformed parameters` section, and the prior and likelihood calculations are performed in the `model` section. Certain vector-valued prior distribution parameters are specified in the `transformed data` section for convenience.

The *Stan* model is then compiled and run (Stan Development Team 2014b) to yield MCMC samples from the posterior distribution of light-curve parameters. We have used PyStan version 2.2.0.[21]

We configured the *No-U-Turn Sampler* to use fixed 0 initialization of the parameter values, an adaptation phase of 250 steps, a maximum tree depth of 22, and otherwise employed the default sampler parameters. Using this configuration, we achieve a Gelman–Rubin between-to-within chain variance ratio of $\hat{R} < 1.02$ for 95% of parameters, indicating excellent convergence. The typical run time is 1 minute per chain.

```
data {
    int<lower=0> N_obs;
    int<lower=0> N_filt;
    vector[N_obs] t;
    vector[N_obs] fL;
    vector[N_obs] dfL;
    real z;
    real t0_mean;
    int<lower=1,upper=N_filt> J[N_obs];
    int<lower=0> Kcor_N;
    real Kcor[N_filt,Kcor_N];
    real<lower=0> fluxscale;
    real<lower=0,upper=1> duringseason;
}
transformed data {
    vector[N_filt] prior_tp;
    vector[N_filt] prior_sig_tp;
    vector[N_filt] prior_lbeta1;
    vector[N_filt] prior_sig_lbeta1;
    vector[N_filt] prior_lbeta2;
    vector[N_filt] prior_sig_lbeta2;
prior_tp[1] <− log(5);
    prior_tp[2] <− log(8);
    prior_tp[3] <− log(14);
    prior_tp[4] <− log(20);
```

```
  prior_tp[5] < − log(30);
  prior_sig_tp[1] < − 0.3;
prior_sig_tp[2] < − 0.3;
  prior_sig_tp[3] < − 0.3;
  prior_sig_tp[4] < − 0.3;
  prior_sig_tp[5] < − 0.3;
prior_lbeta1[1] < − −2.1;
  prior_lbeta1[2] < − −2.3;
  prior_lbeta1[3] < − −3.3;
  prior_lbeta1[4] < − −3.8;
  prior_lbeta1[5] < − −4.0;
prior_sig_lbeta1[1] < − 0.6;
  prior_sig_lbeta1[2] < − 0.8;
  prior_sig_lbeta1[3] < − 1.2;
  prior_sig_lbeta1[4] < − 1.5;
  prior_sig_lbeta1[5] < − 2;
prior_lbeta2[1] < − −3.4;
  prior_lbeta2[2] < − −4;
  prior_lbeta2[3] < − −4.1;
  prior_lbeta2[4] < − −4.4;
  prior_lbeta2[5] < − −4.9;
prior_sig_lbeta2[1] < − 1;
  prior_sig_lbeta2[2] < − 1.2;
  prior_sig_lbeta2[3] < − 1.2;
  prior_sig_lbeta2[4] < − 1.5;
  prior_sig_lbeta2[5] < − 1.5;
}
parameters {
  real pt0;
  vector<lower=0>[N_filt] t1;
  vector<lower=0>[N_filt] t2;
  vector<lower=0>[N_filt] td;
  vector<lower=0>[N_filt] tp;
  vector<upper=0>[N_filt] lalpha;
  vector<upper=0>[N_filt] lbeta1;
  vector<upper=0>[N_filt] lbeta2;
  vector<upper=0>[N_filt] lbetadN;
  vector<upper=0>[N_filt] lbetadC;
  vector<lower=0>[N_filt] Mp;
  vector[N_filt] Yb;
  vector<lower=0>[N_filt] V;
}
transformed parameters {
  vector[N_obs] mm;
  vector[N_obs] dm;
  vector<lower=0>[N_filt] M1;
  vector<lower=0>[N_filt] M2;
  vector<lower=0>[N_filt] Md;
  M1 < − Mp./ exp(exp(lbeta1).* tp);
  M2 < − Mp.* exp(−exp(lbeta2).* t2);
  Md < − M2.* exp(−exp(lbetadN).* td);
  for (n in 1:N_obs) {
    real N_SNc;
    int Kc_up;
    int Kc_down;
    real t_exp;
    int j;
    int k;
    real mm_1;
    real mm_2;
    real mm_3;
    real mm_4;
    real mm_5;
```

```
real mm_6;
j < − J[n];
t_exp < − (t[n] − (t0_mean + pt0)) / (1 + z);
if (t_exp<0) {
mm_1 < − Yb[j];
} else {
mm_1 < − 0; }
if ((t_exp>=0) && (t_exp < t1[j])) { mm_2 < −
    Yb[j] + M1[j] * pow(t_exp / t1[j] , exp(lalpha[j]));
} else {
mm_2 < − 0;
}
if ((t_exp >= t1[j]) && (t_exp < t1[j] +
    tp[j])) {
mm_3      <      −      Yb[j]      +      M1[j]      *
    exp(exp(lbeta1[j]) * (t_exp − t1[j]));
} else {
mm_3 < − 0;
}
if ((t_exp >= t1[j] + tp[j]) && (t_exp < t1[j] + tp[j] +
    t2[j])) {
mm_4 < − Yb[j] + Mp[j] * exp(−exp(lbeta2[j]) *
    (t_exp − t1[j] − tp[j]));
} else {
mm_4 < − 0;
}
if ((t_exp >= t1[j] + tp[j] + t2[j]) && (t_exp < t1[j] +
    tp[j] + t2[j] + td[j])) {
mm_5 < − Yb[j] + M2[j] * exp(−exp(lbetadN[j]) *
    (t_exp − t1[j] − tp[j] − t2[j]));
} else {
mm_5 < − 0;
}
if (t_exp >= t1[j] + tp[j] + t2[j] + td[j]) {
mm_6 < − Yb[j] + Md[j] * exp(−exp(lbetadC[j]) *
    (t_exp − t1[j] − tp[j] − t2[j] − td[j]));
} else {
mm_6 < − 0;
}
dm[n] < − sqrt(pow(dfL[n],2) + pow(V[j],2));
if (t_exp<0) {
N_SNc < − 0;
} else if (t_exp<Kcor_N−2){
Kc_down < − 0;
while ((Kc_down+1) < t_exp) {
Kc_down < − Kc_down + 1;
}
Kc_up < − Kc_down+1;
N_SNc    <     −    Kcor[j,Kc_down+1]    +    (t_exp   −
    floor(t_exp)) * (Kcor[j,Kc_up+1]−Kcor[j,Kc_down+1]);
} else {
N_SNc < − Kcor[j,Kcor_N];
}
mm[n] < − (mm_1+mm_2+mm_3+mm_4+mm_5+mm_6)
/ (pow(10, N_SNc/(−2.5)));
}
}
model {
if (duringseason == 1) {
pt0 ∼ skew_normal(−1, 1, −0.5);
} else {
pt0 ∼ skew_normal(−30, 20, −1);
}
```

```
    t1 ~ lognormal(log(1), 0.3);
    tp ~ lognormal(prior_tp, prior_sig_tp);
    t2 ~ lognormal(log(100), 0.3);
    td ~ lognormal(log(10), 0.5);
    lalpha ~ normal(−1, 0.3);
    lbeta1 ~ normal(prior_lbeta1, prior_sig_lbeta1);
    lbeta2 ~ normal(prior_lbeta2, prior_sig_lbeta2);
    lbetadN ~ normal(−3, 0.5);
    lbetadC ~ normal(−5, 1);
    Mp ~ lognormal(log(1), 0.7);
    Yb ~ normal(0, 0.3);
    V ~ cauchy(0, 0.01);
    fL ~ normal(mm,dm);
}
```

APPENDIX B

LINEAR RELATION WITH INTRINSIC SCATTER *STAN* MODEL

Below we reproduce the full probabilistic model describing a linear relation between bivariate data with intrinsic scatter, which we apply to the SN IIP decline rate–peak magnitude relation in Section 4.6, specified in the *Stan* modeling language and following (Hogg et al. 2010).

The model takes the following data as input: N, the number of bivariate observations; x and y, the mean observed values of the first and second covariates; dx and dy, the uncertainty (standard deviation) of each observation projected along the axis of each covariate; and dxy, the covariance of each observation. In the `transformed parameters` section, the sampled angle of the linear relation from the *x*-axis (`theta`) and its perpendicular distance (`b_perp`) from the origin are used to calculate the perpendicular distance of each observation from the ridgeline of the sampled relation and its projected variance. The prior and likelihood calculations are performed in the `model` section, accounting for both the projected observational variance and the intrinsic variance (`V`). The `b_perp` and `theta` parameters are transformed into traditional linear slope and offset parameters (`m`,`b`) in the `generated quantities` section for convenience.

The *Stan* model is then compiled and run as described in Appendix A.

```
data {
    int<lower=0> N;
    vector[N] x;
    vector[N] y;
    vector[N] dx;
    vector[N] dy;
    vector[N] dxy; }
parameters {
    real<lower=−pi()/2.,upper=pi()/2.> theta;
    real b_perp;
    real<lower=0> V;
}
transformed parameters {
    unit_vector[2] v;
    vector[N] Delta;
    matrix[N,2] Z;
    cov_matrix[2] S[N];
    vector[N] Sigma_squared;
    v[1] < − −sin(theta);
    v[2] < − cos(theta);
    for (n in 1:N) {
        Z[n,1] < − x[n];
        Z[n,2] < − y[n];
        S[n][1,1] < − pow(dx[n],2);
        S[n][2,2] < − pow(dy[n],2);
        S[n][1,2] < − dxy[n];
        S[n][2,1] < − S[n][1,2];
        Sigma_squared[n] < − v' * S[n] * v;
    Delta[n] < − v' * Z[n]' − b_perp;
    }
}
model {
V ~ cauchy(0,2.5);
for (n in 1:N) {
0 ~ normal(Delta[n],sqrt(Sigma_squared[n] + V));
}
}
generated quantities {
real b;
real m;

m < − tan(theta);
b < − b_perp / cos(theta);
}
```

REFERENCES

Aihara, H., Allende Prieto, C., An, D., et al. 2011, ApJS, 193, 29
Anderson, J. P., González-Gaitán, S., Santiago, H.,, et al. 2014, ApJ, 786, 67
Arcavi, I., Gal-Yam, A., Cenko, S. B., et al. 2012, ApJL, 756, L30
Arnett, W. D. 1980, ApJ, 237, 541
Barbon, R., Ciatti, F., & Rosino, L. 1979, A&A, 72, 287
Baron, E., Nugent, P. E., Branch, D., & Hauschildt, P. H. 2004, ApJL, 616, L91
Bersten, M. C., & Hamuy, M. 2009, ApJ, 701, 200
Blanton, M. R., & Roweis, S. 2007, AJ, 133, 734
Cardelli, J. A., Clayton, G. C., & Mathis, J. S. 1989, ApJ, 345, 245
Chieffi, A., Domínguez, I., Höflich, P., Limongi, M., & Straniero, O. 2003, MNRAS, 345, 111
Chugai, N. N., & Utrobin, V. P. 2000, A&A, 354, 557
Clark, D. H., McCrea, W. H., & Stephenson, F. R. 1977, Natur, 265, 318
D'Andrea, C. B., Sako, M., Dilday, B., et al. 2010, ApJ, 708, 661
Dessart, L., & Hillier, D. J. 2011, MNRAS, 410, 1739
Dessart, L., Hillier, D. J., Waldman, R., & Livne, E. 2013, MNRAS, 433, 1745
Dressler, A., Hare, T., Bigelow, B. C., & Osip, D. J. 2006, Proc. SPIE, 6269, 62690F
Drout, M. R., Soderberg, A. M., Gal-Yam, A., et al. 2011, ApJ, 741, 97
Dwarkadas, V. V. 2014, MNRAS, 440, 1917
Ekström, S., Georgy, C., Eggenberger, P., et al. 2012, A&A, 537, A146
Eldridge, J. J. 2008, RSPTA, 366, 4441
Elias-Rosa, N., Van Dyk, S. D., Li, W., et al. 2011, ApJ, 742, 6
Fabricant, D., Fata, R., Roll, J., et al. 2005, PASP, 117, 1411
Faran, T., Poznanski, D., Filippenko, A. V., et al. 2014, MNRAS, 442, 844
Faraway, J., Mahabal, A., Sun, J., et al. 2014, arXiv:1401.3211
Filippenko, A. V. 1997, ARA&A, 35, 309
Foley, R. J., Sanders, N. E., & Kirshner, R. P. 2011, ApJ, 742, 89
Fraser, M., Takáts, K., Pastorello, A., et al. 2010, ApJL, 714, L280
Fryer, C. L. 1999, ApJ, 522, 413
Gelman, A., Carlin, J., Stern, H., et al. 2013, Bayesian Data Analysis, 3rd ed., Chapman & Hall/CRC Texts in Statistical Science (London: Taylor & Francis)
Gelman, A., Jakulin, A., Pittau, M. G., & Su, Y.-S. 2008, AnApS, 2, 1360
Georgy, C., Ekström, S., Eggenberger, P., et al. 2013, A&A, 558, A103
Gezari, S., Rest, A., Huber, M. E., et al. 2010, ApJL, 720, L77
Gilliland, R. L., Nugent, P. E., & Phillips, M. M. 1999, ApJ, 521, 30
Groh, J. H., Meynet, G., & Ekström, S. 2013a, A&A, 550, L7
Groh, J. H., Meynet, G., Georgy, C., & Ekström, S. 2013b, A&A, 558, A131
Hamuy, M. 2003, ApJ, 582, 905
Hamuy, M., & Pinto, P. A. 2002, ApJL, 566, L63
Heger, A., Fryer, C. L., Woosley, S. E., Langer, N., & Hartmann, D. H. 2003, ApJ, 591, 288
Hodapp, K. W., Siegmund, W. A., Kaiser, N., et al. 2004, Proc. SPIE, 5489, 667
Hoffman, M. D., & Gelman, A. 2014, J. Mach. Learn. Res., 15, 1593

Hogg, D. W., Baldry, I. K., Blanton, M. R., & Eisenstein, D. J. 2002, arXiv:astro-ph/0210394

Hogg, D. W., Bovy, J., & Lang, D. 2010, arXiv:1008.4686

Hook, I. M., Jørgensen, I., Allington-Smith, J. R., et al. 2004, PASP, 116, 425

Jerkstrand, A., Smartt, S. J., Fraser, M., et al. 2014, MNRAS, 439, 3694

Kaiser, N., Aussel, H., Burke, B. E., et al. 2002, Proc. SPIE, 4836, 154

Kasen, D., & Woosley, S. E. 2009, ApJ, 703, 2205

Komatsu, E., Smith, K. M., Dunkley, J., et al. 2011, ApJS, 192, 18

Leitherer, C., Robert, C., & Drissen, L. 1992, ApJ, 401, 596

Leonard, D. C., Filippenko, A. V., Gates, E. L., et al. 2002, PASP, 114, 35

Li, W., Leaman, J., Chornock, R., et al. 2011, MNRAS, 412, 1441

Li, W., Wang, X., Van Dyk, S. D., et al. 2007, ApJ, 661, 1013

Lineweaver, C. H., Fenner, Y., & Gibson, B. K. 2004, Sci, 303, 59

Litvinova, I. Y., & Nadezhin, D. K. 1985, SvAL, 11, 145

Magnier, E. 2006, in The Advanced Maui Optical and Space Surveillance Technologies Conference, ed. S. Ryan (Hawaii: The Maui Economic Development Board), E50

Magnier, E. A., Liu, M., Monet, D. G., & Chambers, K. C. 2008, in IAU Symp. 248, A Giant Step: From Milli- to Micro-arcsecond Astrometry, ed. W. J. Jin, I. Platais, & M. A. C. Perryman (Cambridge: Cambridge Univ. Press), 553

Maguire, K., Di Carlo, E., Smartt, S. J., et al. 2010, MNRAS, 404, 981

Maguire, K., Jerkstrand, A., Smartt, S. J., et al. 2012, MNRAS, 420, 3451

Meynet, G., Eggenberger, P., Ekstrom, S., et al. 2013, EAS, 63, 373

Miknaitis, G., Pignata, G., Rest, A., et al. 2007, ApJ, 666, 674

Milisavljevic, D., Margutti, R., Soderberg, A. M., et al. 2013, ApJ, 767, 71

Nadyozhin, D. K. 2003, MNRAS, 346, 97

Nakar, E., & Sari, R. 2010, ApJ, 725, 904

Nomoto, K., Kobayashi, C., & Tominaga, N. 2013, ARA&A, 51, 457

Nomoto, K., Tominaga, N., Umeda, H., Kobayashi, C., & Maeda, K. 2006, NuPhA, 777, 424

Nomoto, K. I., Iwamoto, K., & Suzuki, T. 1995, PhRp, 256, 173

Nugent, P., Sullivan, M., Ellis, R., et al. 2006, ApJ, 645, 841

Olivares, F. 2008, arXiv:0810.5518

Pastorello, A., Zampieri, L., Turatto, M., et al. 2004, MNRAS, 347, 74

Patat, F., Barbon, R., Cappellaro, E., & Turatto, M. 1993, A&AS, 98, 443

Patat, F., Barbon, R., Cappellaro, E., & Turatto, M. 1994, A&A, 282, 731

Pedregosa, F., Varoquaux, G., Gramfort, A., et al. 2011, J. Mach. Learn. Res., 12, 2825

Phillips, M. M., Lira, P., Suntzeff, N. B., et al. 1999, AJ, 118, 1766

Poznanski, D. 2013, MNRAS, 436, 3224

Poznanski, D., Butler, N., Filippenko, A. V., et al. 2009, ApJ, 694, 1067

Rabinak, I., & Waxman, E. 2011, ApJ, 728, 63

Rest, A., Scolnic, D., Foley, R. J., et al. 2014, ApJ, 795, 44

Rest, A., Stubbs, C., Becker, A. C., et al. 2005, ApJ, 634, 1103

Richardson, D., Jenkins, R. L., III, Wright, J., & Maddox, L. 2014, AJ, 147, 118

Sanders, N., Betancourt, M., & Soderberg, A. 2014, arXiv:1404.3619

Sanders, N. E., Levesque, E. M., & Soderberg, A. M. 2013, ApJ, 775, 125

Schmidt, G. D., Weymann, R. J., & Foltz, C. B. 1989, PASP, 101, 713

Scott, D. 1992, Multivariate Density Estimation: Theory, Practice, and Visualization (New York: Wiley)

Smartt, S. J. 2009, ARA&A, 47, 63

Smartt, S. J., Eldridge, J. J., Crockett, R. M., & Maund, J. R. 2009, MNRAS, 395, 1409

Smith, N., Li, W., Filippenko, A. V., & Chornock, R. 2011, MNRAS, 412, 1522

Stan Development Team. 2014a, Stan: A C++ Library for Probability and Sampling, Version 2.2

Stan Development Team. 2014b, Stan Modeling Language Users Guide and Reference Manual, Version 2.2

Stilp, A. M., Dalcanton, J. J., Warren, S. R., et al. 2013, ApJ, 772, 124

Stubbs, C. W., Doherty, P., Cramer, C., et al. 2010, ApJS, 191, 376

Swartz, D. A., Wheeler, J. C., & Harkness, R. P. 1991, ApJ, 374, 266

Takáts, K., Pumo, M. L., Elias-Rosa, N., et al. 2014, MNRAS, 438, 368

Timmes, F. X., Woosley, S. E., & Weaver, T. A. 1995, ApJS, 98, 617

Tonry, J., & Onaka, P. 2009, in Advanced Maui Optical and Space Surveillance Technologies Conference, ed. S. Ryan (Hawaii: The Maui Economic Development Board), E50

Tonry, J. L., Stubbs, C. W., Lykke, K. R., et al. 2012, ApJ, 750, 99

Utrobin, V. P., & Chugai, N. N. 2008, A&A, 491, 507

Walmswell, J. J., & Eldridge, J. J. 2012, MNRAS, 419, 2054

Wang, X., Filippenko, A. V., Ganeshalingam, M., et al. 2009, ApJL, 699, L139

York, D. G., Adelman, J., Anderson, J. E., Jr., et al. 2000, AJ, 120, 1579

Young, T. R. 2004, ApJ, 617, 1233